Trace element partitioning during incipient melting of phlogopite-peridotite in the spinel and garnet stability fields

Authors

Pierre Condamine[1]*, Simon Couzinié[1], Alessandro Fabbrizio[2], Jean-Luc Devidal[3], Etienne Médard[3]

Affiliations

[1]*Université de Lorraine, CNRS, CRPG, F-54000 Nancy, France*

[2]*Institute of Petrology and Structural Geology, Faculty of Science, Charles University, Albertov 6, 12843 Prague, Czech Republic*

[3]*Université Clermont Auvergne, CNRS, IRD, OPGC, Laboratoire Magmas et Volcans, F-63000 Clermont-Ferrand, France*

Correspondence (*)

pierre.condamine@univ-lorraine.fr

Abstract

Potassium-rich magmatism represents subordinate magma volumes worldwide but has been observed in many geodynamic settings. Most potassic magmas are thought to derive from very-low degrees of melting of metasomatized mantle lithologies. We performed piston-cylinder experiments to determine trace element partition coefficients between incipient potassic silicate melts and phlogopite ± pargasite peridotite in the spinel (1 GPa) and garnet stability fields (3 GPa). Most of the rare Earth elements (REEs) are compatible in pargasite but incompatible in phlogopite. Although garnet remains the mineral phase most efficiently fractionating heavy from light REEs

$(D_{Yb}^{grt/melt}/D_{La}^{grt/melt} > 750)$, orthopyroxene can also significantly fractionate REEs, e.g., achieving $D_{Yb}^{opx/melt}/D_{La}^{opx/melt} > 100$ at 3 GPa. Mineral-liquid partition coefficients vary by about one order of magnitude between incipient melts derived from the spinel and garnet stability fields. We thus show that trace element partitioning at the onset of melting is controlled more by pressure (through melt composition) than by the extent of melting. With increasing pressure, Rb and Ba exhibit different behaviors in phlogopite, with $D_{Ba}^{phl/melt}>D_{Rb}^{phl/melt}$ at 1 GPa and the opposite at 3 GPa. At 1 GPa, a decrease of melt polymerization (lower NBO/T) with increasing melt fraction translates into a significant decrease of most phlogopite partition coefficients. Finally, we show that resolvable inter-element fractionations do occur when phlogopite- (and pargasite)-bearing peridotite are melted, indicating that trace element ratios are not always faithfully representative of that of their sources but bear the imprint of varied P–T conditions of melting and contrasted pre-metasomatic histories. This self-consistent partition coefficient dataset thus gives a new scope to understand the complex petrogenesis of K-rich magmas in orogenic settings.

Keywords

Phlogopite | Pargasite | Partitioning | Incipient melt | Rare Earth Elements | K-rich magmas

1. Introduction

Potassic magmatism, i.e., igneous rock series typified by elevated K_2O contents and K_2O/Na_2O > 1 at > 3 wt. % MgO (Foley et al., 1987; Nelson, 1992), is observed in a wide variety of geodynamic settings, ranging from intraplate to orogenic. Iconic examples include the subduction-related Roman volcanic province (Rogers et al., 1985; Foley, 1992; Schiano et al., 2004; Gaeta et al., 2011), Pliocene potassic magmas from the Sierra Nevada, California (Van Kooten 1980; Feldstein and Lange 1999), post-collisional "shoshonites" erupted in Anatolia, Tibet and Taïwan (Harris et al., 1994; Chung et al., 1995; Williams et al., 2004; Prelević et al., 2012) and their plutonic counterparts well-exposed in the

Variscan belt (vaugnerites and durbachites; Holub, 1997; Couzinié et al., 2016; Janoušek et al., 2020) or even the pre-shield stage of Kilauea (Sisson et al., 2009).

The elevated MgO and transition metal (Ni, Cr) contents of primitive potassic magmas necessarily require the melting of an ultramafic source (peridotite, pyroxenite). However, their elevated K_2O/Na_2O ratios and overall high large-ion lithophile elements (LILE, e.g., K, Rb, Cs, Sr, Ba) concentrations are generally interpreted as reflecting the presence of hydrous, alkali-bearing phases (e.g., pargasite and phlogopite) in the mantle source (e.g., Foley et al., 1987; Turner et al., 1996; Williams et al., 2004; Prelević et al., 2012). Indeed, the atypical trace element incompatibility order of K-rich magmas is inconsistent with the melting of dry peridotite (Schiano et al., 2004). Importantly, the ubiquitous LILE enrichment and common high field strength element (HFSE, e.g., Nb, Ta) depletions in potassic magmas recall the signatures of arc magmatic suites (Pearce, 1982; LaTourette et al., 1995; Schiano et al., 2004), emphasizing the subduction-related origin of the hydrous phases in their mantle sources (Schiano et al., 2004; Williams et al., 2004). Because K-rich igneous rocks very often display "crust-like" (i.e., radiogenic Sr, unradiogenic Nd and Hf) isotopic compositions (Nelson, 1992; Couzinié et al., 2016), it is argued that such hydrous phases formed by interactions between sediment-derived metasomatic melts (and/or supercritical fluids) and ultramafic rocks. This view is supported by the natural occurrence of phlogopite (±pargasite)-bearing peridotites in orogenic massifs (e.g., the Finero body; Zanetti et al., 1999) and the results of silicic melt/peridotite interaction experiments (Sekine and Wyllie, 1982; Prouteau et al., 2001; Mallik et al., 2015; Förster et al., 2019).

Several experimental studies have demonstrated the effects of hydrous mantle minerals on the geochemical signatures of primary melts, for example showing that LILEs have a greater affinity for phlogopite than pargasitic amphibole (Guo and Green, 1990; Adam et al., 1993; LaTourette et al., 1995). Furthermore, LaTourette et al. (1995) and Adam and Green (2006) observed that the partition coefficients of trace elements, especially REEs, are systematically lower in phlogopite than in pargasitic amphibole. Importantly, previous experiments on trace element partitioning between phlogopite and silicate melts have only been performed on lamproitic (Guo and Green, 1990; Adam

et al., 1993; Schmidt et al., 1999; Fabbrizio et al., 2010) and basanitic melt compositions (LaTourette et al., 1995; Green et al., 2000; Adam and Green, 2006) whereas post-collisional potassic to ultrapotassic magmas in Tibet, Anatolia, Taiwan and the Variscan Belt of Western Europe (Pearce and Houjun, 1988; Harris et al., 1994; Chung et al., 2001; Lustrino and Wilson, 2007; Martin et al., 2017) are mostly trachyandesitic. . Besides, despite their wide use in characterizing magma sources and fractionation paths, experimental data on REE partitioning in phlogopite are very sparse (Adam and Green, 2006; Fabbrizio et al., 2010).

Most models developed to reconcile the trace and major element compositions of potassic to ultrapotassic igneous rocks invoke low degrees of melting of a metasomatized mantle source (e.g., Turner et al., 1996; Williams et al., 2004; Martin et al., 2017). It is thus important to determine partition coefficients for melt compositions representative of incipient melts derived from metasomatized mantle sources and to better document the role of hydrous, alkali-bearing mantle minerals in trace element partitioning. In this study, we report the results of experiments performed to determine the partition coefficients of a wide variety of trace elements in K-rich low-degree melts in equilibrium with phlogopite ± pargasite lherzolite. Experiments were conducted in piston-cylinder apparatuses at 1 and 3 GPa and between 1040 and 1250 °C to investigate the effects of pressure and melt composition on trace element partitioning, and to derive a self-consistent partition coefficient dataset with direct applicability to the genesis of potassic to ultrapotassic igneous rocks.

2. Methods

2.1. Starting materials

The bulk starting materials used in each experiment included a target potassic melt composition (72–100 wt. %) and a model peridotite composition (28–0 wt. %). The three melt compositions at 1 GPa (Table 1) were chosen to determine trace element partition coefficients between phlogopite lherzolite and trachyte to basaltic trachy-andesite melts, corresponding to very-low (melt composition Lhz1050, f = 4.4 wt. %, where f is the weight fraction of melt), low (melt

composition Lhz1075, f = 6.3 wt. %, where f is the weight fraction of melt) and to moderate (Lhz1150, f = 11.8 wt. %) degrees of equilibrium melting at 1 GPa (Condamine and Médard, 2014). We also investigated trace element partitioning in a phonotephrite (Table 1), representing a low-degree melt (3Lhz1250, f = 3.9 wt. %) derived from phlogopite lherzolite at 3 GPa (Condamine et al., 2016).

The model metasomatized lherzolite composition (Table 1) is a mix of 90 wt. % Bri5 peridotite and 10 wt. % natural phlogopite from the Finero ultramafic massif (Italy). Bri5 is a spinel lherzolite xenolith from Mont Briançon (France) comprising 62.6 wt. % olivine, 22.8 wt. % orthopyroxene, 12.4 wt. % clinopyroxene and 2.2 wt. % spinel. The detailed composition and preparation of the phlogopite lherzolite are described in Condamine and Médard (2014). In some experiments, small amounts of coarse (~ 50µm) phlogopite, olivine, orthopyroxene and clinopyroxene crystals from the Bri5 peridotite were added as seeds to promote crystallization.

Melt compositions were prepared by mixing analytical grade oxides (SiO_2, TiO_2, Al_2O_3, Cr_2O_3, Fe_2O_3, and MgO) and synthetic mineral powders (fayalite, pseudowollastonite, albite, and orthoclase). The $Fe^{3+}/\Sigma Fe$ ratio was fixed to 0.1 in the synthetic melt composition to fit natural mantle xenolith values (Frost and McCammon, 2008), using the model of Kress and Carmichael (1991). Mixtures were ground in ethanol for 30 min and dried at 400 °C for 24 h. Twenty-six trace elements were added to the mixture as liquid solutions to obtain individual trace element concentrations of about 150 ppm for Co; 300 ppm for Li, Be, B, Sc, Rb, Sr, Y, Nb, La, Ce, Nd, Sm, Eu, Gd, Dy, Ho, Yb, Lu and Ta; and 600 ppm for V, Zr, Ba, Hf, Th, and U. The total amount of added trace oxides was about 0.96 wt. %. The spiked powder was mixed in water for 45 min and dried at 600 °C for 2 h to evaporate residual nitric and hydrochloric acids from the elemental solutions. Water was then added as $Al(OH)_3$ powder and mixed in dry conditions. Starting materials were stored in an oven at 110 °C. The melt composition was added to the phlogopite lherzolite to conduct sandwich-like experiments, with the melt corresponding to 72–100 wt. % of the bulk composition, of which ~20 wt. % was inserted as a thick layer in the middle of the capsule to facilitate glass analyses and the rest was mixed into the lherzolite to enhance the attainment of equilibrium and mineral growth.

2.2. Experimental procedure

Experiments at 1 GPa were performed at 1040–1140 °C for durations of 80–145 h (Table 2) in a 19.1-mm piston-cylinder apparatus at the Laboratoire Magmas et Volcans (LMV, Clermont-Ferrand, France), using the Lhz1050, Lhz1075 and Lhz1150 starting melt compositions, respectively. Experiments at a nominal pressure of 3 GPa were performed at 1250 °C for 89 h in an end-loaded 12.7-mm piston-cylinder apparatus in the same laboratory, using the 3Lhz1250 starting melt composition. Our assemblies comprised a NaCl cell wrapped in an outer lead foil, a Pyrex cylinder, a graphite furnace and inner MgO spacers. We used calibrated $W_{74}Re_{26}$-$W_{95}Re_5$ thermocouples to control temperature to within 1 °C of the setpoint. The temperature gradient in our capsule setup is about 15 °C (Sorbadere et al. 2013). To promote crystal growth, experiments were first held at 1050, 1075, 1150, or 1250°C for 1 h; the temperature was then oscillated by ±5 °C around the target temperature with ramps of 0.2 °C/h, and the experiments were held for 6 h between oscillations. The last 24 h of experiments at 1 GPa were then performed at 10 °C below the target temperature (i.e., 1040, 1065 or 1140 °C) to enhance crystal growth. The experiments were terminated by shutting off the power, leading to quench rates of ~50 °C/s and ~175 °C/s in the 19.1-mm and 12.7-mm piston-cylinders, respectively (Laporte et al., 2004; Médard et al., 2006).

Experiments at 1040–1065 °C were performed using Au single capsules. $Au_{90}Pd_{10}$ double capsule setups were required for experiments at 1140 °C and 1250 °C. The outer capsule was filled with the same glass composition as the inner capsule to prevent Fe loss and H diffusion (Kägi et al., 2005), as well as to check the doping efficiency during preparation of the starting materials (tr07e, Table S1). To minimize H_2O adsorption, packed capsules were placed in an oven at 110 °C during 24 h then quickly welded shut.

2.3. Analytical techniques

After the experimental runs, capsules were sectioned lengthwise, embedded in epoxy and polished on nylon pads. We used a Cameca SX100 electron microprobe at the LMV to determine the major element compositions of melts and minerals (Table 3) and to locate large mineral grains for laser ablation inductively coupled plasma mass spectrometry (LA-ICP-MS) analyses. For anhydrous crystalline phases, we used a focused beam with a 15 kV accelerating voltage, a 15 nA current, and on-peak and background counting times of 10 s. For glasses and hydrous minerals, the beam current was lowered to 8 nA and the beam was defocused to a diameter of 5–20 μm. A mean of five analyses was performed for mineral phases and at least 10 analyses were performed for glassy melts. Mineral and melt proportions were determined by mass balance (Albarède and Provost, 1977).

To determine the water contents of experimental glasses, Raman spectroscopy was performed at GeoRessources (Nancy, France) with a LabRAM HR spectrometer (Horiba Jobin Yvon) coupled to an argon ion laser (wavelength 514.53 nm) using a focused beam to obtain a 1 μm-wide spot under a 50x objective. A low laser power was used (10 mW) and regularly checked to reduce the excitation volume and prevent water loss. All spectra were collected at the sample surface with counting times of 50 s: in each of the 150–1400 cm^{-1} (alumino-silicate network domain) and 2800-4000 cm^{-1} (OH + H_2O domain) Raman shift ranges. During Raman sessions, a standard sample was regularly analyzed to detect any shift in laser intensity. Due to the compositional dependence of band intensities during Raman spectroscopy (e.g., Mercier et al., 2009), we used synthetic standards with compositions similar to those of our melts (see supplementary materials of Condamine and Médard, 2014). The spectra were treated with a cubic fit to the baseline (Di Muro et al., 2009) using PeakFit software. Most glass pools produced high fluorescence, precluding H_2O quantification in silicate melts due to the interaction of REEs with the laser (Panczer et al., 2012).

Trace element concentrations in glasses and minerals were determined using an Agilent 7500cs ICP-MS coupled to a 193 nm Excimer Resonetics M-50E laser ablation system at the LMV. We analyzed 32 masses (^{7}Li, ^{24}Mg, ^{27}Al, ^{29}Si, ^{44}Ca, ^{45}Sc, ^{47}Ti, ^{51}V, ^{53}Cr, ^{55}Mn, ^{59}Co, ^{60}Ni, ^{85}Rb, ^{88}Sr, ^{89}Y, ^{90}Zr,

^{93}Nb, ^{137}Ba, ^{139}La, ^{140}Ce, ^{146}Nd, ^{147}Sm, ^{153}Eu, ^{157}Gd, ^{163}Dy, ^{165}Ho, ^{172}Yb, ^{175}Lu, ^{178}Hf, ^{181}Ta, ^{232}Th, and ^{238}U)

with integration times of 30 and 60 ms per mass in glasses and minerals, respectively, except for

^{24}Mg, ^{27}Al, ^{29}Si and ^{44}Ca (10 ms). The laser fluence was 2.8 J/cm^2 and pulse frequencies were 2 and 4

Hz for minerals and glasses, respectively. We used beam sizes of 15 and 70 μm for minerals and

glasses, respectively. Backgrounds were collected during the first 30 s, followed by laser ablation of

the samples during 60 s. Ca and Al abundances measured by electron microprobe were used as

internal standards for melt and mineral phases, respectively. We used NIST 610 (Pearce et al., 1997;

Gagnon et al., 2008) as an external standard. To assess the accuracy of our analyses, we also used

NIST 612 and BCR-2G as secondary standards (Gagnon et al., 2008; Sigmarsson et al., 2013). After the

LA-ICP-MS sessions, every laser pit was checked on the microprobe to ensure the reliability of the

analyses. Trace element concentrations were then computed using Glitter software to monitor the

stability of the signal intensity through time. We also re-analyzed an unspiked melting experiment of

Condamine and Médard (2014; sta12) performed using a natural starting material at 1 GPa and 1050

°C for trace elements.

Because melts from experiments at 3 GPa did not quench to glassy pools, we analyzed them

by LA-ICP-MS to obtain their representative major element compositions (Humayun et al., 2010;

Davis et al., 2011; Tenner et al., 2012). We used a laser frequency of 3 Hz and a beam size ranging

between 20 and 70 μm. We first collected the background for 30 s, then the laser was fired on the

sample for 60 s. We used NIST-610 (Pearce et al., 1997; Gagnon et al., 2008), BCR (Wilson, 1997), BIR

(Flanagan, 1984) and ATHO (Jochum et al., 2000) as standards. Relative sensitivity factors (Humayun

et al., 2007) were calculated avoiding elements present in trace amounts in the glass standards.

3. Results

3.1. Textures and equilibrium

Typical experimental textures are illustrated in Figure 1. Overall, the experiments contained a

high proportion of silicate glass (27–67 wt. %) (Table 2). The synthetic glass composition inserted

between peridotite layers was preserved in all sandwich experiments. At 1 GPa, most of the olivine and clinopyroxene present in the starting material was consumed to form pargasite via the reaction olivine + clinopyroxene + spinel + melt = pargasite + orthopyroxene (Médard and Schmidt, 2008). Pargasite was present in all experiments performed at 1040–1065 °C but absent at 1140 °C; in the experiment reanalyzed from Condamine and Médard (2014), pargasite was stable at 1050 °C (Table 2).

In our experiments, the olivine–melt Fe–Mg exchange coefficient $K_D{}_{Fe-Mg}^{ol-melt}$ ranged between 0.21 and 0.35, in good agreement with theoretical exchange coefficients computed using the model of Toplis (2005). The clinopyroxene–melt Fe–Mg exchange coefficient $K_D{}_{Fe-Mg}^{cpx-melt}$ varied between 0.37 and 0.44, slightly higher than the average $K_D{}_{Fe-Mg}^{cpx-melt}$ = 0.28 ± 0.08 reported by Putirka (2008). In orthopyroxene, $K_D{}_{Fe-Mg}^{opx-melt}$ values (0.29 ± 0.06) were comparable to those reported by Putirka (2008). Temperatures calculated using the clinopyroxene–melt and orthopyroxene–melt geothermometers of Putirka (2008) are identical within errors to the nominal experimental temperatures. According to previous experiments using the same setup (Condamine and Médard, 2014; Condamine et al., 2016), the experimental fO$_2$ should have ranged between FMQ and FMQ + 1 (FMQ reference from O'Neill, 1987). The loss or gain of iron and water were estimated in all experiments by mass balance (Table 2). Except for experiment tr10e, Fe losses/ gains varied between -4.8 and +9.7% relative to the starting Fe contents, negligible considering the uncertainties on the compositions of the starting materials and final run products. Water losses/gains ranged between -3.6 and +5.7% relative to the starting H$_2$O contents, within the analytical errors of Raman spectroscopy.

3.2. Mineral and melt compositions

Mineral and melt compositions analyzed by microprobe are reported in Table 3. The compositions of melts in the middle layers of the sandwich experiments did not significantly shift

compared to those of their starting materials, further indicating near-equilibrium conditions. In experiments at 1040–1065 °C, silicate melts were trachytic. At 1140 °C, melts were identical to the starting material within error, apart from their higher Na_2O contents (2.5 vs. 1.8 wt. % in tr07). In experiments at 3 GPa and 1250 °C, melts were tephritic and contained systematically less K_2O than the starting glass composition. Melt compositions in the outer capsules of 3 GPa experiments tr09e and tr10e were phonotephritic.

Olivine grains were always very small (< 10 μm) and difficult to analyze. Orthopyroxene (enstatite) was present in all experiments except tr09e and tr10e (both at 3 GPa) and contained 1.5–6.3 wt. % Al_2O_3 and 0.2–1.3 wt. % CaO. Clinopyroxene was diopside at 1 GPa and shifted to augite at 3 GPa, reflecting a decrease in CaO content, from 19.7–21.1 wt. % at 1 GPa to 16.3–18.1 wt. % at 3 GPa. Garnet (Mg# = 0.80–0.82, 5.3 wt. % CaO) was only present in experiments tr10 and tr10e (3 GPa, 1250 °C). Phlogopite was ubiquitous in all experiments, with Mg# = 0.86–0.94. Phlogopite TiO_2 contents varied significantly between experiments, from 1.2 wt. % (tr04) to 4.6 wt. % (sta16). The Na_2O content of phlogopite decreased from 0.5–1.3 wt. % at 1 GPa to 0.3–0.4 wt. % at 3 GPa, whereas K_2O content increased from 8.8–9.9 wt. % at 1 GPa to 10.2–10.6 wt. % at 3 GPa. Pargasitic amphibole (9.7–11.4 wt. % CaO, 2.6–3.8 wt. % Na_2O) was only present in experiments at 1040–1065 °C and 1 GPa.

3.3. Trace element partition coefficients

Partition coefficients determined between phlogopite and incipient melts derived from phlogopite-bearing peridotite are reported in Table 4 and plotted to show the range in partition coefficients between experiments at a given pressure in Figure 2. In these experiments, LILEs (Rb, Ba, K) are compatible with phlogopite, except for Sr, which is moderately incompatible. Ba is less compatible at 3 GPa ($D_{Ba}^{phl/melt}$ = 1.3–1.7) than at 1 GPa ($D_{Ba}^{phl/melt}$ = 3.2–6.3). Of the HFSEs, only Ti is compatible with phlogopite, and only at 1 GPa ($D_{Ti}^{phl/melt}$ = 2.6–6.7); it becomes slightly incompatible at 3 GPa ($D_{Ti}^{phl/melt}$ = 0.7). Zr, Nb, Hf, and Ta are moderately incompatible at 1 GPa and become

more incompatible with increasing pressure. Similarly, Th and U are incompatible at 1 GPa and become more incompatible at 3 GPa. REEs are more incompatible at higher pressure, with $D_{REE}^{phl/melt}$ < 0.1 at 1 GPa and $D_{REE}^{phl/melt}$ < 0.01 at 3 GPa. Phlogopite slightly fractionates heavy and light REEs (HREEs and LREEs, respectively), especially at higher pressure, with $D_{Yb}^{phl/melt}/D_{La}^{phl/melt}$ ranging between 6 and 15 at 3 GPa. Of the first-row transition elements (FRTEs), Cr, Co and Ni are compatible at both 1 and 3 GPa; Mn is sometimes compatible at 1 GPa and becomes incompatible with increasing pressure ($D_{Mn}^{phl/melt}$ = 0.2 at 3 GPa). In contrast to the other FRTEs, V is incompatible at 1 GPa ($D_{V}^{phl/melt}$ = 0.02–0.96) and becomes less incompatible to slightly compatible at 3 GPa ($D_{V}^{phl/melt}$ = 0.2–1.6).

Partition coefficients determined between pargasite and melts are reported in Table 4 and Figure 3. In contrast to phlogopite, LILEs are incompatible in pargasite ($D_{LILE}^{prg/melt}$ = 0.03–0.6). HFSE partition coefficients are comparable to those in phlogopite, with only Ti being compatible in pargasite ($D_{Ti}^{prg/melt}$ = 2.0–3.8), and Zr, Nb, Hf, and Ta being moderately incompatible. Th and U are less incompatible in pargasite than in phlogopite and are slightly fractionated (on average, $D_{Th}^{prg/melt}$ = 0.04 and $D_{U}^{prg/melt}$ = 0.01). Among the LREEs, only La and Ce are moderately incompatible, whereas Nd, Sm, Eu, and Gd are slightly incompatible to compatible in pargasite. HREEs are compatible in pargasite at 1040–1050 °C, but slightly incompatible ($D_{HREE}^{prg/melt}$ > 0.6) at 1065 °C (sta19). Pargasite slightly fractionates LREEs and HREEs, with $D_{Yb}^{prg/melt}/D_{La}^{prg/melt}$ > 5. FRTEs (except V) are compatible with pargasite.

Partition coefficients obtained between clinopyroxene and melts are reported in Table 4 and Figure S1a. LILEs are highly incompatible at both 1 and 3 GPa. HFSEs are also incompatible, especially Nb, Ta, Th, and U, which have partition coefficients <0.03 at 1 GPa and <0.01 at 3 GPa. LREEs are highly incompatible at 1 and 3 GPa, whereas HREEs are moderately incompatible; in both cases, incompatibility increases with increasing pressure. The fractionation of LREEs from HREEs is limited in clinopyroxene, with $D_{Yb}^{cpx/melt}/D_{La}^{cpx/melt}$ = 7–13 at both 1 and 3 GPa. Except for V, FRTEs are

compatible with clinopyroxene at 1 GPa, whereas at 3 GPa, Ni and Cr are compatible, and Mn and Co are not.

Partition coefficients determined between orthopyroxene and melts are reported in Table 4 and Figure S1b. Overall, LILEs are highly incompatible in orthopyroxene. We only determined $D_{Sr}^{opx/melt}$ at 3 GPa, which indicates that incompatibility increases with increasing pressure. As in pargasite, REEs are incompatible in orthopyroxene, except for Sc, which is compatible to slightly incompatible at 1 GPa ($D_{Sc}^{opx/melt}$ = 0.7–2.4). Like in other mineral phases, REEs are more incompatible with increasing pressure. Moreover, in orthopyroxene, HREEs are fractionated from LREEs, and this fractionation increases with increasing pressure: $D_{Yb}^{opx/melt}/D_{La}^{opx/melt}$ = 6–43 at 1 GPa and reaches 120–141 at 3 GPa. FRTEs are highly compatible in orthopyroxene, but become less so with increasing pressure: $D_{Mn}^{opx/melt}$ > 1.5 at 1 GPa and >0.6 at 3 GPa.

Only experiments tr10 and tr10e produced garnet; in those experiments, we determined partition coefficients between garnet and melts, which are reported in Table 4 and Figure S1c. Both LILEs and HFSEs are extremely incompatible in garnet, with $D_{LILE}^{grt/melt}$ < 0.004 and $D_{HFSE}^{grt/melt}$ < 0.1. LREEs are also highly incompatible; e.g., $D_{La}^{grt/melt}$ = 0.0015–0.0060. In contrast, HREEs are compatible; e.g., $D_{Yb}^{grt/melt}$ = 4.5. This leads to fractionation factors of $D_{Yb}^{grt/melt}/D_{La}^{grt/melt}$ = 750 and 2,700 in tr10e and tr10, respectively. Among FRTEs, only Ni is slightly incompatible; Cr, Mn, and Co are compatible in garnet.

4. Discussion

4.1. Lattice strain models

Elemental partitioning between minerals and melts is partly dependent on crystal chemistry (Blundy and Wood, 1994, 2003). Elements are incorporated into crystal sites according to their ionic radii and charges. In this section, we test the reliability of our experimental dataset by fitting Onuma diagrams (Onuma et al., 1968). The partitioning of isovalent cations is described by the lattice strain

model, in which the mineral/melt partition coefficient D_i of element i with ionic radius r_i, entering a specific crystallographic site is compared to the partition coefficient D_0 of an 'ideal' element with an ionic radius r_0 equivalent to that of the host site as (Brice, 1975; Blundy and Wood, 1994, 2003):

$$D_i = D_0 \exp\left(\frac{-910.17E}{T}\left(\frac{r_0}{2}(r_i - r_0)^2 + \frac{1}{3}(r_i - r_0)^3\right)\right), \qquad (1)$$

where E is the apparent Young's modulus (GPa) of the site of interest and T is temperature (K). Equation (1) applies to isovalent series of elements entering the same crystallographic site. The three parameters D_0, r_0, and E determine the apex (r_0, D_0) and width (E) of an asymmetric parabola for that crystallographic site. That is, E is a measure of the elastic response of the crystallographic site to strain on the crystal lattice caused by elements of non-ideal size, and thus describes that site's flexibility (Blundy and Wood, 2003).

Equation (1) is also used to evaluate the quality of an experimental dataset and to estimate D values for elements that were not investigated. It may also be used to estimate the ideal D values of elements at low concentrations, i.e., highly incompatible elements, in cases where their detection is problematic due to analytical uncertainties and/or potential contamination by microscopic melt inclusions (e.g., van Kan Parker et al., 2011; Dygert et al., 2020). Moreover, the distribution coefficients of highly incompatible elements, i.e., $D \leq 10^{-3}$, may be influenced by defect substitutions, surface kinetics, and boundary layers in the melt, rendering their experimental determination difficult to impossible (Beattie, 1994; Pinilla et al., 2012).

Furthermore, the lattice strain model can give information on the partitioning of specific elements between multiple sites (e.g., Ba in pargasites; Tiepolo et al., 2007) or on their dominant valence in the case of heterovalent elements (e.g., Eu in plagioclase, Aigner-Torres et al., 2007; Eu in pyroxene, Fabbrizio et al., 2021). In such cases, elements fall off the parabolas defined by elements that substitute exclusively into a given site with a given valency (Dygert et al., 2020). We used the DOUBLE and SIMPLE FIT programs of Dalou et al. (2018) to determine the D_0, r_0, and E for each experimental charge. We will use the resulting parabolas in D vs. ionic radius space to assess how well our experimental data fit the lattice strain model.

Phlogopite is a trioctahedral mica with the ideal formula $KMg_3AlSi_3O_{10}(OH)_2$. We were only able to fit a lattice strain parabola to the divalent cations entering the 12-coordinated interlayer (X) site in the few cases where we measured the partition coefficients of the alkaline-Earth metals Ca, Sr, and Ba. An additional difficulty lies in the fact that these elements plot to the left of the parabolic fit (Figure 4) and thus potentially poorly constrain the lattice strain parameters. The values we obtained for E are comparable to those of previous works in which D_{Ca}, D_{Sr}, and D_{Ba} were measured (Table S1; Schmidt et al., 1999; Fabbrizio et al., 2010) and, as expected, these values are larger than those obtained for phlogopite in Ra-bearing experiments (Fabbrizio et al., 2010). This difference stems from the fact that the ionic radius of Ra puts it slightly to the right of the parabola, and thus better constrains the parabola's width (Fabbrizio et al., 2010). For monovalent cations hosted in the interlayer site, the absence of Cs did not allow us to accurately define the lattice strain parameters; we thus assumed $E^{1+} = E^{2+}/2$. With this assumption, K and Rb plot near the apexes and Na on the left limbs of the resulting parabolas. We also note that Li partition coefficients plot off the parabolas for monovalent cations suggesting that, due to its smaller ionic radius, Li enters the octahedral (VI-fold) M1 and M2 sites (Brigatti and Guggenheim, 2002). Parabolic fits of divalent cations show that they are hosted in the octahedral sites. Because their partition coefficients define the right limb of the M2 parabola, Mg, Co, Fe, and Mn are hosted in the same octahedral site M2. In contrast, D_{Ni} values plot off the M2 parabola, suggesting that Ni enters the M1 site. Trivalent cations enter the octahedral sites (Blundy and Wood, 2003) and are fractionated between the M1 (Al, Sc) and M2 sites (REEs). However, the high incompatibility of REEs in phlogopite, coupled with the high uncertainties related to the measurement of their partition coefficients and kinetic effects during crystal growth, prevented us from obtaining a parabolic trend as a function of their ionic radii. Consequently, we could not determine lattice strain parameters for REEs in the M2. Conversely, the partition coefficients of Al and Sc plot on both sides of the M1 parabola, permitting us to obtain a good constraint for their lattice strain parameters in the M1 site. Tetravalent cations are fractionated

between the VI-fold octahedral sites M1 and M2, with Ti, Zr, and Hf entering the M1 site and Th and U entering the M2 site. The phlogopite lattice strain parameters reported in Table S1 are within the range of literature values (Icenhower and London, 1995; Schmidt et al., 1999; Fabbrizio et al., 2010).

4.1.2. Pargasite

Pargasite is an amphibole with the ideal formula $NaCa_2(Mg_4Al)Si_6Al_2O_{22}(OH)_2$. The good parabolic fit obtained for the partition coefficients of trivalent elements (i.e., REEs, Sc, Al) indicates that pargasite crystallized under near-equilibrium conditions (Figure 5). One of the three structurally distinct octahedral (VI-fold) sites, M1, M2, or M3 hosts Sc and Al, whereas REEs enter the larger VIII-fold M4 and M4' sites. Because the apexes of the parabolic fits for most of our experiments are located between the ionic radii of Dy and Tb, REEs should preferentially occupy the M4' site (Bottazzi et al., 1999; Tiepolo et al., 2000). Eu partition coefficients plot on the REE parabolas, indicating that all Eu is trivalent in our experiments. The parabolic fits for divalent elements suggest that Ca and Sr enter the larger (XII-fold) A site, whereas smaller cations enter the M4 site along with Mg, which seems to be fractionated between the VIII-fold and VI-fold sites. Ni enters exclusively into the smaller VI-fold site. However, because the partition coefficients of these elements plot only on one side of the respective parabolas, we did not obtain good constraints on the lattice strain parameters for the sites of interest. The parabolic fits for monovalent cations indicate that they are incorporated in the larger A site, providing a very good constraint on its lattice strain parameters. Tetravalent cations are fractionated between the VIII-fold (U, Th) and VI-fold sites (Ti, Zr, Hf). The pargasite lattice strain parameters are reported in Table S1 and are within the range of literature (Blundy and Wood, 2003). The hybrid model of Shimizu et al. (2017), based on the major element compositions of both pargasite and melt, reproduces the measured REE partition coefficients well (Figure S3).

4.1.3. Clinopyroxene

The parabolic distribution of trivalent (i.e., REEs, Sc, and Al^{IV}) partition coefficients indicates that clinopyroxene in all runs crystallized under near-equilibrium conditions (Figure 6). In all runs, Eu partition coefficients plot on the parabolas defined by REEs, suggesting that Eu is again only present

as a trivalent cation. The M1 site hosts only Sc and ^{IV}Al, and the lesser flexibility of the M1 compared to the M2 site is evidenced by the tighter parabolas defined by these elements (i.e., $E^{3+}_{M1} > E^{3+}_{M2}$). Ba partition coefficients were excluded from the fits for divalent elements because they are characterized by high uncertainties and systematically plot off the parabolas defined by more compatible divalent elements (Figure 6). It was not possible to constrain the lattice strain parameters for the M1 site because all divalent elements entering the M1 site plot on the same side of the parabola (Dalou et al., 2018). Tetravalent elements fractionate between the M1 (Ti, Hf, Zr) and M2 sites (U, Th), defining tighter parabolas due to their higher charges. Figure 6 reports the fitted lattice strain parameters for isovalent elements entering the same site, showing that they are similar among all experiments. The model of Sun and Liang (2012) reproduces our measured REE partition coefficients very well (Figure S3).

4.1.4. Orthopyroxene

Isovalent elements in orthopyroxene describe parabolic trends with features similar to those observed for clinopyroxene (Figure 7). However, the apexes of trivalent parabolas for REEs in the M2 site are not well defined because these elements plot to the right of the parabolic fits. Eu partition coefficients again plot on the REE parabolas, showing that all Eu is trivalent. Small trivalent cations are preferentially incorporated into the M1 site, as indicated by the tighter parabola than that for larger trivalent cations partitioning into the M2 site (e.g., Frei et al., 2008; van Kan Parker et al., 2010; Sun and Liang, 2013a). In many cases the model of Yao et al. (2012) does not reproduce the distribution coefficients of the most incompatible REEs, suggesting contamination by microscopic melt inclusions and/or kinetic effects during crystal growth. The REE distribution coefficients that deviate most from the model of Yao et al. (2012) are not considered representative of equilibrium conditions and were excluded from the fits (Figure S3). The M2 site is occupied by larger divalent cations defining broad parabolas. Ba partition coefficients again have high uncertainties and are well above the values predicted by the parabolas (~10^{-4}), and were thus excluded from the fits. As in clinopyroxene, tetra-valent cations fractionate between the M1 and M2 sites and define the tightest

parabolas with the highest E values, as also observed by Sun and Liang (2013a). The lattice strain parameters for orthopyroxenes (Table S1) are within the range of values obtained previously (e.g., Yao et al., 2012; Sun and Liang, 2013a; Dygert et al., 2020).

4.1.5. Garnet

The parabolic distributions of REEs and Sc indicate that these trivalent elements enter the dodecahedral (VIII-fold) X site (Figure S2). The apexes of these parabolas are well defined because Sc and Lu plot on the left and right sides of the parabolas, respectively. Eu partition coefficients plot between those of Sm and Gd, once again confirming that all Eu is present as Eu^{3+}. The model of Sun and Liang (2013b, 2014) tends to slightly overestimate the REE distribution coefficients (Figure S3). The X site hosts all divalent cations and its lattice strain parameters are well constrained because larger (i.e., Ca and Sr) and smaller cations plot on the right and left sides of the parabolas, respectively, and Mn near the apexes of the parabolas. Ba partition coefficients were excluded from the fits because they are very low ($<<10^{-4}$) and characterized by high uncertainties. The well-defined E^{2+} values permitted us to derive E^{1+} values (again assuming $E^{1+} = E^{2+}/2$) that, in combination with D_{Li} and D_{Na} values, constrain the apexes of the parabolic fits for monovalent cations in the X site. Larger tetravalent cations (U, Th) enter the X site whereas smaller ones (Ti, Hf, Zr) preferentially enter the octahedral (VI-fold) Y site. However, because U and Th plot on the same side of the parabolic fits, the lattice strain parameters for the X site are not well constrained. Garnet lattice strain parameters are reported in Table S1 and are within the range of values obtained previously (van Westrenen et al., 1999, 2000a,b).

4.2. Causes of the variable trace element partitioning

Partition coefficients obtained in this study vary greatly between experiments (sometimes by an order of magnitude at a given pressure; Figures 2, 3, S1). Many studies have highlighted that trace element partitioning between mafic melts and minerals is mainly controlled by mineral composition (Blundy and Wood, 1994; Gaetani and Grove, 1995; Blundy et al., 1996; Wood and Blundy, 1997;

Adam and Green, 2003). However, melt composition, and more specifically the degree of polymerization (reflected by NBO/T, with lower values indicating more polymerized melts; Mysen, 1983) should also influence partitioning, particularly in highly polymerized melts (NBO/T < 0.5; Gaetani, 2004; Mysen, 2004; Huang et al., 2006; Schmidt et al., 2006).

Our dataset offers the opportunity to evaluate this effect because the degree of melt polymerization varied significantly between our different experiments conducted at a given pressure, whereas mineral major element compositions remained nearly constant (Table S1). At 1 GPa, trachytic melts from experiments at 1040–1050 °C were highly polymerized (NBO/T = 0.11–0.17, Table 2). Melt polymerization was lower in experiment sta19 at 1065 °C (NBO/T = 0.22) and further decreased in experiments at 1140 °C (with the melt reaching a trachy-andesitic composition and NBO/T = 0.35 in experiment tr07). At 3 GPa, incipient melts were more depolymerized, with NBO/T = 0.76 for the phonotephrites in tr09e and tr10e and NBO/T = 0.93–0.96 for the tephrites in tr09 and tr10.

The evolution of some phlogopite–melt trace element partition coefficients as a function of melt polymerization is shown in Figure 8. For example, at 1 GPa, $D_{Yb}^{phl/melt}$ ranges between 0.016 and 0.036 in the most highly polymerized trachytic melts but decreases to 0.003 in higher-T trachy-andesitic compositions at the same pressure. Similar patterns are observed for several elements that are highly (Ni) to moderately (Ti) and poorly (Sr) compatible in phlogopite (Figure 8). In contrast, partition coefficients obtained in experiments at 3 GPa (which generated depolymerized tephritic to phonotephritic melts) do not vary as a function of NBO/T. These results strongly recall those of Gaetani (2004) for clinopyroxene and further indicate NBO/T = 0.5 as a threshold above which melts are sufficiently depolymerized to negligibly influence trace element partitioning (Hirschmann et al., 1999; Gaetani, 2004).

Therefore, phlogopite–melt partition coefficients evolve from incipient (generating strongly polymerized melts) to higher degrees of melting. This effect should be restricted to relatively shallow

(<1.5 GPa) partial melting in the Earth's mantle because peridotite-derived melts formed at higher pressures always exhibit NBO/T > 0.5 (Gaetani, 2004).

4.3. Trace element systematics of melts derived from phlogopite (and amphibole)-bearing peridotites

Here, we build upon our new and self-consistent partition coefficient dataset to explore the trace element compositions of potassic mantle-derived melts in equilibrium with residual phlogopite ± pargasite. Notably, we aim to identify the extents to which pressure, modal composition, and degrees of melting control trace element partitioning between melt and residue and the occurrence of geochemical "anomalies", i.e., the selective enrichment or depletion of a (or a group of) trace element(s) with respect to others. This discussion is particularly relevant to petrogenetic studies of potassic magmatic rocks because trace element ratios are very commonly used to fingerprint the composition and origin of a metasomatic agent in the mantle source (e.g., Guo et al., 2013; Liu et al., 2014) without consideration of potential fractionations attributable to the melting assemblage. To address this aspect, we implemented a non-modal batch melting model (see caption of Figure 9 for details on the model parameters) at 1 and 3 GPa based on previously determined melting equations for low-degree melting of phlogopite (± pargasite)-bearing peridotite (Condamine and Médard, 2014; Condamine et al., 2016).

We considered two model sources with contrasting major-element concentrations (one fertile, one depleted) to cover the range of potential upper mantle endmember compositions and to estimate how the presence of clinopyroxene (and amphibole) may affect the trace element systematics of phlogopite peridotite-derived melts. These sources correspond to the starting materials BriPhl and HzbPhl used in the experiments of Condamine and Médard (2014) and Condamine et al. (2016). BriPhl is a fertile phlogopite-bearing lherzolite that also contains amphibole at 1 GPa (but not at 3 GPa) whereas HzbPhl is a depleted clinopyroxene-free phlogopite-bearing harzburgite. In both

compositions spinel and garnet are the aluminous phases at 1 and 3 GPa, respectively. Calculations were performed using an R script adapted from Janoušek et al. (2016) and the results plotted in Figure 9 and 10 via GCDKit (Janoušek et al., 2006).

Our model results show that melt Th, U, Zr, Hf, Sr, and LREE concentrations are primarily controlled by the degree of melting, attaining melt/source enrichments of 30–50 and 8–10 at 2 and 10 wt. % melt, respectively. In contrast, the partitioning of MREEs (Sm, Eu, Gd), HREEs (Dy, Yb), Ti, Rb, Ba, and to a lesser extent, Nb between melt and residue varies as a function of pressure and source composition. Specifically, the stability of clinopyroxene and pargasite at 1 GPa in fertile peridotite (BriPhl) restricts the transfer of MREEs and HREEs to the melt compared to more depleted sources (HzbPhl); melt/source MREE and HREE enrichments in phlogopite + pargasite lherzolite are 40–80% lower than those in phlogopite harzburgite at 10 wt. % melt. Calculations performed on a pargasite-free BriPhl composition (Figure S4) indicate that LREE/MREE fractionation is mainly caused by the crystallization of clinopyroxene, consistent with the low modal abondance of pargasite in BriPhl (3.4 wt. %). This effect is more subtle at 3 GPa due to the lower partition coefficients of MREEs in clinopyroxene.

Pressure strongly influences the behaviors of (i) Ti, (ii) Ba and Rb, (iii) MREEs and HREEs, and (iv) Nb. First, Ti is compatible with phlogopite at 1 GPa, and its presence in the residue restricts Ti transfer to the melt (melt/source ratio: 1.7–5.0), generating a negative Ti anomaly (here quantified by the ratio Sm_N/Ti_N, where the subscript 'N' denotes normalization to the source composition), the amplitude of which is stronger in depleted compositions (Sm_N/Ti_N = 1–4 in BriPhl but 1–14 in HzbPhl). At 3 GPa, Ti is less compatible with phlogopite, leading to higher concentrations of Ti in the melt and weaker negative Ti anomalies (Sm_N/Ti_N = 1–3 for both source compositions). Second, the compatibility of Ba and Rb with phlogopite and the reversal of the magnitude of their respective partition coefficients with increasing pressure ($D_{Ba}^{phl/melt} > D_{Rb}^{phl/melt}$ at 1 GPa, the opposite at 3 GPa) is predicted to cause their selective depletion relative to other trace elements in melts (Ba_N/La_N = 0.1–1) and a pressure-dependent Ba–Rb fractionation (Ba_N/Rb_N = 0.6–1.0 at 1 GPa and 2.2–1.0 at 3

GPa). Third, the strong MREE/HREE fractionation observed in melts at 3 GPa reflects the presence of garnet in the residue, as largely documented in phlogopite-free compositions (e.g., Salters and Longhi, 1999). Interestingly, low-degree (f < 6 wt. %) melts produced at 1 GPa in depleted pargasite- and clinopyroxene-free harzburgites are expected to show only a slight MREE/HREE fractionation (Sm_N/Yb_N = 1.5–2.2, compared to Sm_N/Yb_N = 4.2–11.1 at 3 GPa) because orthopyroxene exerts a strong control on the budget of these elements and $D_{Yb}^{opx/melt}/D_{Sm}^{opx/melt}$ > 6 at 1 GPa. Finally, our modelling predicts the generation of a weak negative Nb anomaly in low-degree (f < 6 wt. %) melts from both fertile and depleted compositions at 1 GPa only (Th_N/Nb_N = 1.4–2.4).

For a given melt fraction, the amount of phlogopite being present in the source at the onset of melting has little to no impact on the melt uptake of most trace elements, with the notable exceptions of Rb, Ba and Ti (Figure 10). Indeed, their concentrations in the melt phase may vary by nearly one order of magnitude depending on the phlogopite mode, thus leading to strong inter element fractionations under specific conditions. For instance, considering a 6 wt. % melt fraction, Ba_N/La_N drops from 0.57 down to 0.09 when the mode of phlogopite in the lherzolite source increases from 4 to 20 wt. %. A similar situation is observed at 1 and 3 GPa regardless of the lherzolite or harzburgite nature of the phlogopite-bearing source (Figure S5).

Collectively, these results highlight resolvable inter-element fractionations during the melting of phlogopite (±pargasite)-bearing peridotite. Primary melts inherit trace element ratios that may not exclusively represent those of their source, but may also bear the imprint of the P–T conditions during melting and/or the modal mineralogy (phlogopite mode, presence of clinopyroxene and/or amphibole). Therefore, variations among trace element ratios (such as Ba/La, Ba/Th, Th/Nb, Rb/Ba) in a suite of rock samples with (near-)primary compositions may not necessarily require the existence of several, chemically distinct sources.

4.4. Application to a naturel dataset of potassic magmatic rocks: unveiling source compositions

Potassic magmatic rocks are conspicuous in post-collisional orogenic settings where they define "high-K calc-alkaline" to "shoshonite" series (Couzinié et al., 2016 and references therein). Even though it is generally advocated that their parental melts were derived from metasomatized phlogopite-bearing peridotites (e.g., Turner et al., 1996), few natural samples among these suites exhibit primitive melt compositions due to the combined effect of crystal fractionation, hybridization with cognate (or not) magmas and possibly assimilation within the crust (Williams et al., 2004; Prelević et al., 2012; Guo et al., 2013; Liu et al., 2014). In this section, we illustrate how the newly obtained self-consistent partitioning dataset can be used to unravel the nature and trace element systematics of the source of potassic suites when selectively applied to primitive melt compositions. We proceed by: (i) interrogating a database of potassic rocks from the Variscan French Massif Central to screen out "primitive" samples; (ii) comparing their major element compositions with available experimental data to derive reasonable assumptions on the mineralogy of the source and the melting degree f; (iii) using the partitioning dataset and the non-modal batch melting model developed section 4.3 to back-calculate the trace element composition of their mantle source(s).

In the French Massif Central, potassic rocks include deep-seated (mid-crustal) stocks of K-rich (monzo-)diorites, termed vaugnerites, and dykes of lamprophyres (mostly kersantites) intrusive at higher structural levels (Sabatier, 1991). Both were emplaced at c. 335–300 Ma following the main collisional phase of the Variscan orogeny and attest to a lithospheric mantle melting event presumably triggered by heat conduction from the asthenosphere (Laurent et al., 2017), A compilation of available geochemical data for such rocks (n = 367) was published in Couzinié et al. (2016). Primitive samples (equilibrated with the mantle) were identified by applying the criteria of Schmidt and Jagoutz (2017), i.e., bulk rock Mg# between 65–75 and Ni contents in the range 150–500 ppm. Following this, one lamprophyre (sample SGC-12-13) and one vaugnerite (sample SC-13-05), both fully characterized in Couzinié et al. (2016), were selected for further modelling.

The lamprophyre sample has an intermediate composition (SiO_2 = 53.4 wt. %) with low CaO (5.3 wt. %) and Na_2O (1.5 wt. %) but high K_2O contents (4.8 wt. %) together with a low CaO/Al_2O_3 ratio of 0.38. Thus, it strikingly resembles the melts formed at the expense of phlogopite harzburgite at 1 GPa but for which phlogopite was exhausted from the melting assemblage (Figure 11a,b, Condamine and Médard, 2014). For the vaugnerite sample, lower SiO_2 (51.8 wt. %) and K2O (3.3 wt. %) contents but higher CaO (6.7 wt. %), Na2O (2.2 wt. %), and a CaO/Al_2O_3 ratio of 0.52 rather indicate that the source was a phlogopite lherzolite and that here again, phlogopite was not part of the 1 GPa melting residue. In the experiments of Condamine and Médard (2014) conducted at 1 GPa, the exhaustion of phlogopite was observed for a temperature of c. 1200 °C. However, the geologic record of the French Massif Central, and notably P–T estimates available from lower crustal granulites scavenged by Cenozoic volcanoes (Downes and Leyreloup, 1986) clearly indicate that such elevated temperatures were not prevailing at depths of c. 35–40 km (corresponding to 1 GPa) during the time interval inferred for the lithospheric mantle melting event. Therefore, the exhaustion of phlogopite in the mantle source(s) of both samples must have been reached at lower temperatures which necessarily required that they contained less phlogopite than used by Condamine and Médard (2014) in their experimental starting material, i.e., < 10 wt. %.

In the following, we assume that the mantle sources of the lamprophyre and vaugnerite samples contained 6 wt. % phlogopite. Given the stoichiometry of the melting reactions at 1 GPa, phlogopite exhaustion occurs for a melt fraction of 9 wt. % in the model phlogopite harzburgite and 12 wt. % in the model phlogopite lherzolite. Considering that the lamprophyre and the vaugnerite represent such 9 and 12 wt. % primary melts, the trace element composition of their sources can be calculated using the melt/source ratios obtained via the non-modal batch melting model (see section 4.3). The results are depicted in Figure 11c. The primitive mantle-normalized patterns of the two calculated sources are very alike, the source of the vaugnerite being slightly more enriched in MREE, HREE and Ti than that of the lamprophyre. Both sources are typified by their strong enrichment in Rb, Ba, Th, U with respect to the primitive mantle, their marked Nb and Ti negative anomalies, and

slightly fractionated HREE pattern. These results refine earlier estimates (Couzinié et al., 2016) and show that the mantle source of potassic rocks from the French Massif Central resembles a mixture of 85% Depleted Mantle (Workman and Hart, 2005) and 15% of Global Subducting Sediment (GLOSS, Plank and Langmuir, 1998) or the average composition of post-Archean granulite-facies terrains (Hacker et al., 2015), thus placing constraints on the chemical signature of the metasomatic agent.

By providing a more accurate treatment of trace element partitioning during metasomatized mantle melting, our self-consistent partition coefficient dataset offers new opportunities to unravel the complex crust-mantle interactions and associated mantle enrichment in orogenic settings.

5. Conclusions

We performed experiments to determine trace element partition coefficients at the onset of melting of a metasomatized (phlogopite ± pargasite-bearing) peridotite in the spinel and garnet stability fields. For all melt compositions, partition coefficients in phlogopite are systematically lower than those in pargasite, except for LILEs. Trachytic compositions, representing low-degree melts from a metasomatized mantle at 1 GPa, exhibit higher trace element partition coefficients than in previous experimental studies. Together with data from trachyandesitic to tephritic compositions representing higher degrees of melting, this highlights the non-negligible evolution of both melt composition and trace element partitioning during incipient mantle melting. However, partition coefficients are most influenced by the pressure of melting, implying a strong difference between melt compositions at 1 and 3 GPa. This is mainly due to the shift in the incongruent melting reaction of peridotite from orthopyroxene-consuming at <1.5 GPa to olivine-consuming at greater depths in the Earth's mantle. Finally, first-order batch melting models illustrate how residual phlogopite (±pargasite) should imprint the trace element budget of primary, potassic, mantle-derived melts: specific mineral phases produce significant MREE/Ti, Ba/Rb, or Ba/HFSE fractionations.

This new experimental, self-consistent dataset is of primary interest for the further modeling of the wide variety of potassium-rich magmas described worldwide, which, in turn, will allow for a

better understanding of deep volatile cycles (mainly H_2O, CO_2, and F). Because most of these magmas are silica-rich polymerized melts, their elemental partition coefficients are expected to shift during melting events, implying low to moderate degrees of melting. Finally, this dataset will be useful in modelling complex multi-step polybaric scenarios, e.g., as have been proposed for lamproite genesis via the melting of a phlogopite-rich source and subsequent equilibration with the surrounding mantle (e.g., Fan et al., 2021).

References

Adam J. and Green D. H. (2003) The influence of pressure, mineral composition and water on trace element partitioning between clinopyroxene, amphibole and basanitic melts. *Eur. J. Mineral.* **15**, 831–841.

Adam J. and Green T. (2006) Trace element partitioning between mica- and amphibole-bearing garnet lherzolite and hydrous basanitic melt: 1. Experimental results and the investigation of controls on partitioning behaviour. *Contrib. Mineral. Petr.* **152**, 1–17.

Adam J., Green T. H. and Sie S. H. (1993) Proton microprobe determined partitioning of Rb, Sr, Ba, Y, Nb and Ta between experimentally produced amphiboles and silicate melts with variable F content. *Chem. Geol.* **109**, 29–49.

Aigner-Torres M., Blundy J., Ulmer P. and Pettke T. (2007) Laser Ablation ICPMS study of trace element partitioning between plagioclase and basaltic melts: an experimental approach. *Contrib. Mineral. Petr.* **153**, 647–667.

Albarède F. and Provost A. (1977) Petrological and geochemical mass-balance equations: An algorithm for least-square fitting and general error analysis. *Comput. Geosci.* **3**, 309–326.

Beattie P. (1994) Systematics and energetics of trace-element partitioning between olivine and silicate melts: Implications for the nature of mineral/melt partitioning. *Chem. Geol.* **117**, 57–71.

Blundy J. D., Wood B. J. and Davies A. (1996) Thermodynamics of rare earth element partitioning between clinopyroxene and melt in the system CaO-MgO-Al$_2$O$_3$-SiO$_2$. *Geochim. Cosmochim. Ac.* **60**, 359–364.

Blundy J. and Wood B. (2003) Partitioning of trace elements between crystals and melts. *Earth Planet. Sc. Lett.* **210**, 383–397.

Blundy J. and Wood B. (1994) Prediction of crystal-melt partition-coefficients from elastic-moduli. *Nature* **372**, 452–454.

Bottazzi P., Tiepolo M., Vannucci R., Zanetti A., Brumm R., Foley S. F. and Oberti R. (1999) Distinct site preferences for heavy and light REE in amphibole and the prediction of Amph/LDREE. *Contrib. Mineral. Petr.* **137**, 36–45.

Brenan J. M., Shaw H. F., Ryerson F. J. and Phinney D. L. (1995) Experimental determination of trace-element partitioning between pargasite and a synthetic hydrous andesitic melt. *Earth Planet. Sc. Lett.* **135**, 1–11.

Brice J. C. (1975) Some thermodynamic aspects of the growth of strained crystals. *J. Cryst. Growth* **28**, 249–253.

Brigatti M. F. and Guggenheim S. (2002) Mica Crystal Chemistry and the Influence of Pressure, Temperature, and Solid Solution on Atomistic Models. *Rev. Mineral. Geochem.* **46**, 1–97.

Chung S.-L., Wang K.-L., Crawford A. J., Kamenetsky V. S., Chen C.-H., Lan C.-Y. and Chen C.-H. (2001) High-Mg potassic rocks from Taiwan: implications for the genesis of orogenic potassic lavas. *Lithos* **59**, 153–170.

Chung S.-L., Yang T. F., Lee C.-Y. and Chen C.-H. (1995) The igneous provinciality in Taiwan: consequence of continental rifting superimposed by Luzon and Ryukyu subduction systems. *J. Southe. Asian Earth* **11**, 73–80.

Condamine P. and Médard E. (2014) Experimental melting of phlogopite-bearing mantle at 1 GPa: Implications for potassic magmatism. *Earth Planet. Sc. Lett.* **397**, 80–92.

Condamine P., Médard E. and Devidal J.-L. (2016) Experimental melting of phlogopite-peridotite in the garnet stability field. *Contrib. Mineral. Petr.* **171**, 95.

Couzinié S., Laurent O., Moyen J.-F., Zeh A., Bouilhol P. and Villaros A. (2016) Post-collisional magmatism: Crustal growth not identified by zircon Hf–O isotopes. *Earth Planet. Sc. Lett.* **456**, 182–195.

Dalou C., Boulon J., T. Koga K., Dalou R. and Dennen R. L. (2018) DOUBLE FIT: Optimization procedure applied to lattice strain model. *Comput. Geosci.* **117**, 49–56.

Dalpé C. and Baker D. R. (2000) Experimental investigation of large-ion-lithophile-element-, high-field-strength-element- and rare-earth-element-partitioning between calcic amphibole and basaltic melt: the effects of pressure and oxygen fugacity. *Contr. Mineral. and Petrol.* **140**, 233–250.

Davis F. A., Hirschmann M. M. and Humayun M. (2011) The composition of the incipient partial melt of garnet peridotite at 3 GPa and the origin of OIB. *Earth Planet. Sc. Lett.* **308**, 380–390.

Di Muro A., Métrich N., Mercier M., Giordano D., Massare D. and Montagnac G. (2009) Micro-Raman determination of iron redox state in dry natural glasses: Application to peralkaline rhyolites and basalts. *Chem. Geol.* **259**, 78–88.

Downes H. and Leyreloup A. (1986) Granulitic xenoliths from the French Massif Central—petrology, Sr and Nd isotope systematics and model age estimates. *Geol. Soc. London Spec. Publ.* **24**, 319.

Dygert N., Draper D. S., Rapp J. F., Lapen T. J., Fagan A. L. and Neal C. R. (2020) Experimental determinations of trace element partitioning between plagioclase, pigeonite, olivine, and lunar basaltic melts and an fO_2 dependent model for plagioclase-melt Eu partitioning. *Geochim. Cosmochim. Ac.* **279**, 258–280.

Fabbrizio A., Schmidt M. W., Günther D. and Eikenberg J. (2010) Ra-partitioning between phlogopite and silicate melt and ^{226}Ra/Ba–^{230}Th/Ba isochrons. *Lithos* **114**, 121–131.

Fabbrizio A., Schmidt M. W. and Petrelli M. (2021) Effect of fO_2 on Eu partitioning between clinopyroxene, orthopyroxene and basaltic melt: Development of a Eu^{3+}/Eu^{2+} oxybarometer. *Chem. Geol.* **559**, 119967.

Fan W., Jiang N., Hu J., Liu D., Zhao L. and Li T. (2021) A metasomatized ^{18}O-rich veined lithospheric mantle source for ultrapotassic magmas. *Lithos* **382–383**, 105964.

Feldstein S. N. and Lange R. A. (1999) Pliocene Potassic Magmas from the Kings River Region, Sierra Nevada, California: Evidence for Melting of a Subduction-Modified Mantle. *J. Petrol.* **40**, 1301–1320.

Flanagan F. J. (1984) Three USGS mafic rock reference samples, W-2, DNC-1, and BIR-1., US Government Printing Office.

Foley S. (1992) Petrological characterization of the source components of potassic magmas: geochemical and experimental constraints. *Lithos* **28**, 187–204.

Foley S. F., Venturelli G., Green D. H. and Toscani L. (1987) The ultrapotassic rocks: Characteristics, classification, and constraints for petrogenetic models. *Earth-Sci. Rev.* **24**, 81–134.

Förster M. W., Buhre S., Xu B., Prelević D., Mertz-Kraus R. and Foley S. F. (2019) Two-Stage Origin of K-Enrichment in Ultrapotassic Magmatism Simulated by Melting of Experimentally Metasomatized Mantle. *Minerals* **10**, 41.

Frei D., Liebscher A., Franz G., Wunder B., Klemme S. and Blundy J. (2008) Trace element partitioning between orthopyroxene and anhydrous silicate melt on the lherzolite solidus from 1.1 to 3.2 GPa and 1,230 to 1,535°C in the model system Na_2O–CaO–MgO–Al_2O_3–SiO_2. *Contrib. Mineral. Petr.* **157**, 473.

Frost D. J. and McCammon C. A. (2008) The Redox State of Earth's Mantle. *Annu. Rev. Earth Pl. Sc.* **36**, 389–420.

Gaeta M., Freda C., Marra F., Di Rocco T., Gozzi F., Arienzo I., Giaccio B. and Scarlato P. (2011) Petrology of the most recent ultrapotassic magmas from the Roman Province (Central Italy). *Lithos* **127**, 298–308.

Gaetani G. A. (2004) The influence of melt structure on trace element partitioning near the peridotite solidus. *Contrib. Mineral. Petr.* **147**, 511-527.

Gaetani G. A. and Grove T. L. (1995) Partitioning of rare earth elements between clinopyroxene and silicate melt Crystal-chemical controls. *Geochim. Cosmochim. Ac.* **59**, 1951–1962.

Gagnon J. E., Fryer B. J., Samson I. M. and Williams-Jones A. E. (2008) Quantitative analysis of silicate certified reference materials by LA-ICPMS with and without an internal standard. *J. Anal. At. Spectrom.* **23**, 1529–1537.

Green T. H., Blundy J. D., Adam J. and Yaxley G. M. (2000) SIMS determination of trace element partition coefficients between garnet, clinopyroxene and hydrous basaltic liquids at 2-7.5 GPa and 1080-1200°C. *Lithos* **53**, 165–187.

Guo J. and Green T. H. (1990) Experimental study of barium partitioning between phlogopite and silicate liquid at upper-mantle pressure and temperature. *Lithos* **24**, 83–95.

Guo Z., Wilson M., Zhang M., Cheng Z. and Zhang L. (2013) Post-collisional, K-rich mafic magmatism in south Tibet: constraints on Indian slab-to-wedge transport processes and plateau uplift. *Contrib. Mineral. Petr.* **165**, 1311–1340.

Hacker B. R., Kelemen P. B. and Behn M. D. (2015) Continental Lower Crust. *Annu. Rev. Earth Pl. Sc.* **43**, 167–205.

Harris N. B. W., Kelley S. and Okay A. I. (1994) Post-collision magmatism and tectonics in northwest Anatolia. *Contrib. Mineral. Petr.* **117**, 241–252.

Hirschmann M. M., Ghiorso M. S. and Stolper M. (1999) Calculation of Peridotite Partial Melting from Thermodynamic Models of Minerals and Melts. II. Isobaric Variations in Melts near the Solidus and owing to Variable Source Composition. *J. Petrol.* **40**, 297–313.

Hofmann A. W. (1988) Chemical differentiation of the Earth: the relationship between mantle, continental crust, and oceanic crust. *Earth Planet. Sc. Lett.* **90**, 297–314.

Holub F. V. (1997) Ultrapotassic plutonic rocks of the durbachite series in the Bohemian Massif: Petrology, geochemistry and petrogenetic interpretation. *Sborník Geologických Věd, Ložisková Geologie Mineralogie* **31**, 5–26.

Huang F., Lundstrom C. and McDonough W. (2006) Effect of melt structure on trace-element partitioning between clinopyroxene and silicic, alkaline, aluminous melts. *Am. Mineral.* **91**, 1385–1400.

Humayun M., Davis F. A. and Hirschmann M. M. (2010) Major element analysis of natural silicates by laser ablation ICP-MS. *J. Anal. At. Spectrom.* **25**, 998–1005.

Humayun M., Simon S. B. and Grossman L. (2007) Tungsten and hafnium distribution in calcium–aluminum inclusions (CAIs) from Allende and Efremovka. *Geochim. Cosmochim. Ac.* **71**, 4609–4627.

Icenhower J. and London D. (1995) An experimental study of element partitioning among biotite, muscovite, and coexisting peraluminous silicic melt at 200 MPa (H_2O). *Am. Mineral.* **80**, 1229–1251.

Janoušek V., Farrow C. M. and Erban V. (2006) Interpretation of Whole-rock Geochemical Data in Igneous Geochemistry: Introducing Geochemical Data Toolkit (GCDkit). *J. Petrol.* **47**, 1255–1259.

Janoušek V., Hanžl P., Svojtka M., Hora J. M., Kochergina Y. V. E., Gadas P., Holub F. V., Gerdes A., Verner K., Hrdličková K., Daly J. S. and Buriánek D. (2020) Ultrapotassic magmatism in the heyday of the Variscan Orogeny: the story of the Třebíč Pluton, the largest durbachitic body in the Bohemian Massif. *Int. J. Earth Sci.* **109**, 1767–1810.

Janoušek V., Moyen J.-F., Martin H., Erban V. and Farrow C. (2016) Progressive Melting of a Metasedimentary Sequence: the Saint-Malo Migmatitic Complex, France. In *Geochemical Modelling of Igneous Processes – Principles And Recipes in R Language: Bringing the Power of R to a Geochemical Community* (eds. V. Janoušek, J.-F. Moyen, H. Martin, V. Erban, and C. Farrow). Springer Berlin Heidelberg, Berlin, Heidelberg. pp. 261–275.

Jochum K. P., Dingwell D. B., Rocholl A., Stoll B., Hofmann A. W., Becker S., Besmehn A., Bessette D., Dietze H. J., Dulski P., Erzinger J., Hellebrand E., Hoppe P., Horn I., Janssens K., Jenner G. A., Klein M., McDonough W. F., Maetz M., Mezger K., Müker C., Nikogosian I. K., Pickhardt C., Raczek I., Rhede D., Seufert H. M., Simakin S. G., Sobolev A. V., Spettel B., Straub S., Vincze L., Wallianos A., Weckwerth G., Weyer S., Wolf D. and Zimmer M. (2000) The Preparation and Preliminary Characterisation of Eight Geological MPI-DING Reference Glasses for In-Situ Microanalysis. *Geostand. Newsl.* **24**, 87–133.

Kägi R., Müntener O., Ulmer P. and Ottolini L. (2005) Piston-cylinder experiments on H_2O undersaturated Fe-bearing systems: An experimental setup approaching fO_2 conditions of natural calc-alkaline magmas. *Am. Mineral.* **90**, 708–717.

van Kan Parker M., Liebscher A., Frei D., van Sijl J., van Westrenen W., Blundy J. and Franz G. (2010) Experimental and computational study of trace element distribution between orthopyroxene and anhydrous silicate melt: substitution mechanisms and the effect of iron. *Contrib. Mineral. Petr.* **159**, 459–473.

van Kan Parker M., Mason P. R. D. and van Westrenen W. (2011) Experimental study of trace element partitioning between lunar orthopyroxene and anhydrous silicate melt: Effects of lithium and iron. *Chem. Geol.* **285**, 1–14.

Klein M., Stosch H.-G. and Seck H. A. (1997) Partitioning of high field-strength and rare-earth elements between amphibole and quartz-dioritic to tonalitic melts: an experimental study. *Chemical Geology* **138**, 257–271.

Kress V. C. and Carmichael I. S. E. (1991) The compressibility of silicate liquids containing Fe_2O_3 and the effect of composition, temperature, oxygen fugacity and pressure on their redox states. *Contrib. Mineral. Petr.* **108**, 82–92.

Laporte D., Toplis M. J., Seyler M. and Devidal J.-L. (2004) A new experimental technique for extracting liquids from peridotite at very low degrees of melting: application to partial melting of depleted peridotite. *Contrib. Mineral. Petr.* **146**, 463–484.

LaTourrette T., Hervig R. L. and Holloway J. R. (1995) Trace element partitioning between amphibole, phlogopite, and basanite melt. *Earth Planet. Sc. Lett.* **135**, 13–30.

Laurent O., Couzinié S., Zeh A., Vanderhaeghe O., Moyen J.-F., Villaros A., Gardien V. and Chelle-Michou C. (2017) Protracted, coeval crust and mantle melting during Variscan late-orogenic evolution: U–Pb dating in the eastern French Massif Central. *Int. J. Earth Sci.* **106**, 421–451.

Liu D., Zhao Z., Zhu D.-C., Niu Y., DePaolo D. J., Harrison T. M., Mo X., Dong G., Zhou S., Sun C., Zhang Z. and Liu J. (2014) Postcollisional potassic and ultrapotassic rocks in southern Tibet: Mantle and

crustal origins in response to India–Asia collision and convergence. *Geochim. Cosmochim. Ac.* **143**, 207–231.

Lustrino M. and Wilson M. (2007) The circum-Mediterranean anorogenic Cenozoic igneous province. *Earth-Sci. Rev.* **81**, 1–65.

Mallik A., Nelson J. and Dasgupta R. (2015) Partial melting of fertile peridotite fluxed by hydrous rhyolitic melt at 2–3 GPa: implications for mantle wedge hybridization by sediment melt and generation of ultrapotassic magmas in convergent margins. *Contrib. Mineral. Petr.* **169**, 1–24.

Martin A. M., Médard E., Righter K. and Lanzirotti A. (2017) Intraplate mantle oxidation by volatile-rich silicic magmas. *Lithos* **292–293**, 320–333.

McDonough W. F. and Sun S. s (1995) The composition of the Earth. *Chemical Geology* **120**, 223–253.

McKenzie D. and O'Nions R. K. (1991) Partial Melt Distributions from Inversion of Rare Earth Element Concentrations. *J. Petrol.* **32**, 1021–1091.

Médard E. and Schmidt M. W. (2008) Composition of low-degree hydrous melts of fertile spinel-or garnet-bearing lherzolite. *Geochim. Cosmochim. Ac.* **72**, A617.

Médard E., Schmidt M. W., Schiano P. and Ottolini L. (2006) Melting of Amphibole-bearing Wehrlites: an Experimental Study on the Origin of Ultra-calcic Nepheline-normative Melts. *J. Petrol.* **47**, 481–504.

Mercier M., Di Muro A., Giordano D., Métrich N., Lesne P., Pichavant M., Scaillet B., Clocchiatti R. and Montagnac G. (2009) Influence of glass polymerisation and oxidation on micro-Raman water analysis in alumino-silicate glasses. *Geochim. Cosmochim. Ac.* **73**, 197–217.

Mysen B. O. (2004) Element partitioning between minerals and melt, melt composition, and melt structure. *Chem. Geol.* **213**, 1–16.

Mysen B. O. (1983) The Structure of Silicate Melts. *Annu. Rev. Earth Pl. Sc.* **11**, 75–97.

Nelson D. R. (1992) Isotopic characteristics of potassic rocks: evidence for the involvement of subducted sediments in magma genesis. *Lithos* **28**, 403–420.

O'Neill H. S. C. (1987) Quartz-fayalite-iron and quartz-fayalite-magnetite equilibria and the free energy of formation of fayalite (Fe_2SiO_4) and magnetite (Fe_3O_4). *Am. Mineral.* **72**, 67–75.

Onuma N., Higuchi H., Wakita H. and Nagasawa H. (1968) Trace element partition between two pyroxenes and the host lava. *Earth Planet. Sc. Lett.* **5**, 47–51.

Panczer G., De Ligny D., Mendoza C., Gaft M., Seydoux-Guillaume A. and Wang X. (2012) Raman and fluorescence. *EMU Notes in Mineralogy* **12**, 61–82.

Pearce J. A. (1982) Trace element characteristics of lavas from destructive plate boundaries. *Andesites*, 525–548.

Pearce J. A. and Houjun M. (1988) Volcanic Rocks of the 1985 Tibet Geotraverse: Lhasa to Golmud. *Philos. Trans. R. Soc. A* **327**, 169–201.

Pearce N. J. G., Perkins W. T., Westgate J. A., Gorton M. P., Jackson S. E., Neal C. R. and Chenery S. P. (1997) A compilation of new and published major and trace element data for NIST SRM 610 and NIST SRM 612 glass reference materials. *Geostand. Newsl.* **21**, 115–144.

Pinilla C., Davis S. A., Scott T. B., Allan N. L. and Blundy J. D. (2012) Interfacial storage of noble gases and other trace elements in magmatic systems. *Earth Planet. Sc. Lett.* **319–320**, 287–294.

Plank T. and Langmuir C. H. (1998) The chemical composition of subducting sediment and its consequences for the crust and mantle. *Chem. Geol.* **145**, 325–394.

Prelević D., Akal C., Foley S. F., Romer R. L., Stracke A. and van Den Bogaard P. (2012) Ultrapotassic Mafic Rocks as Geochemical Proxies for Post-collisional Dynamics of Orogenic Lithospheric Mantle: the Case of Southwestern Anatolia, Turkey. *J. Petrol.* **53**, 1019–1055.

Prouteau G., Scaillet B., Pichavant M. and Maury R. (2001) Evidence for mantle metasomatism by hydrous silicic melts derived from subducted oceanic crust. *Nature* **410**, 197–200.

Putirka K. D. (2008) Thermometers and Barometers for Volcanic Systems. *Rev. Mineral. Geochem.* **69**, 61–120.

Rogers N. W., Hawkesworth C. J., Parker R. J. and Marsh J. R. (1985) The geochemistry of potassic lavas from Vulsini, Central Italy, and implications for mantle enrichment processes beneath the Roman region. *Contrib. Mineral. Petr.* **90**, 244–257.

Sabatier H. (1991) Vaugnerites: special lamprophyre derived mafic enclaves in some Hercynian granites from Western and Central Europe. In *Enclaves and Granite Petrology* pp. 63–81.

Salters V. J. M. and Longhi J. (1999) Trace element partitioning during the initial stages of melting beneath mid-ocean ridges. *Earth Planet. Sc. Lett.* **166**, 15–30.

Schiano P., Clocchiatti R., Ottolini L. and Sbrana A. (2004) The relationship between potassic, calc-alkaline and Na-alkaline magmatism in South Italy volcanoes: A melt inclusion approach. *Earth Planet. Sc. Lett.* **220**, 121–137.

Schmidt K. H., Bottazzi P., Vannucci R. and Mengel K. (1999) Trace element partitioning between phlogopite, clinopyroxene and leucite lamproite melt. *Earth Planet. Sc. Lett.* **168**, 287–299.

Schmidt M. W., Connolly J. A. D. and Bogaerts M. (2006) Element Partitioning: The Role of Melt Structure and Composition. *Science* **312**, 1646–1650.

Schmidt M. W. and Jagoutz O. (2017) The global systematics of primitive arc melts. *Geochem. Geophy. Geosy.* **18,** 2817– 2854.

Sekine T. and Wyllie P. J. (1982) Phase Relationships in the System $KAlSiO_4$ - Mg_2SiO_4 - SiO_2 - H_2O as a Model for Hybridization Between Hydrous Siliceous Melts and Peridotite. *Contrib. Mineral. Petr.* **79**, 368–374.

Shimizu K., Liang Y., Sun C., Jackson C. R. M. and Saal A. E. (2017) Parameterized lattice strain models for REE partitioning between amphibole and silicate melt. *Am. Mineral.* **102**, 2254–2267.

Sigmarsson O., Laporte D., Carpentier M., Devouard B., Devidal J.-L. and Marti J. (2013) Formation of U-depleted rhyolite from a basanite at El Hierro, Canary Islands. *Contrib. Mineral. Petr.* **165**, 601–622.

Sisson T. W., Kimura J. I. and Coombs M. L. (2009) Basanite–nephelinite suite from early Kilauea: carbonated melts of phlogopite–garnet peridotite at Hawaii's leading magmatic edge. *Contrib. Mineral. Petr.* **158**, 803–829.

Sorbadere F., Médard E., Laporte D. and Schiano P. (2013) Experimental melting of hydrous peridotite-pyroxenite mixed sources: Constraints on the genesis of silica-undersaturated magmas beneath volcanic arcs. *Earth Planet. Sc. Lett.* **384**, 42–56.

Sun C. and Liang Y. (2014) An assessment of subsolidus re-equilibration on REE distribution among mantle minerals olivine, orthopyroxene, clinopyroxene, and garnet in peridotites. *Chem. Geol.* **372**, 80–91.

Sun C. and Liang Y. (2013a) Distribution of REE and HFSE between low-Ca pyroxene and lunar picritic melts around multiple saturation points. *Geochim. Cosmochim. Ac.* **119**, 340–358.

Sun C. and Liang Y. (2012) Distribution of REE between clinopyroxene and basaltic melt along a mantle adiabat: effects of major element composition, water, and temperature. *Contrib. Mineral. Petr.* **163**, 807–823.

Sun C. and Liang Y. (2013b) The importance of crystal chemistry on REE partitioning between mantle minerals (garnet, clinopyroxene, orthopyroxene, and olivine) and basaltic melts. *Chem. Geol.* **358**, 23–36.

Sweeney R. J., Green D. H. and Sie S. H. (1992) Trace and minor element partitioning between garnet and amphibole and carbonatitic melt. *Earth Planet. Sc. Lett.* **113**, 1–14.

Sweeney R. J., Prozesky V. and Przybylowicz W. (1995) Selected trace and minor element partitioning between peridotite minerals and carbonatite melts at 18–46 kb pressure. *Geochim. Cosmochim. Ac.* **59**, 3671–3683.

Tenner T. J., Hirschmann M. M. and Humayun M. (2012) The effect of H_2O on partial melting of garnet peridotite at 3.5 GPa. *Geochem. Geophy. Geosy.* **13**, 28.

Tiepolo M., Oberti R., Zanetti A., Vannucci R. and Foley S. F. (2007) Trace-Element Partitioning Between Amphibole and Silicate Melt. *Rev. Mineral. Geochem.* **67**, 417–452.

Tiepolo M., Vannucci R., Bottazzi P., Oberti R., Zanetti A. and Foley S. (2000) Partitioning of rare earth elements, Y, Th, U, and Pb between pargasite, kaersutite, and basanite to trachyte melts: Implications for percolated and veined mantle. *Geochem. Geophy. Geosy.* **1**, 1039.

Toplis M. J. (2005) The thermodynamics of iron and magnesium partitioning between olivine and liquid: criteria for assessing and predicting equilibrium in natural and experimental systems. *Contrib. Mineral. Petr.* **149**, 22–39.

Turner S., Arnaud N., Liu J., Rogers N., Hawkesworth C., Harris N., Kelley S., van Calsteren P. and Deng W. (1996) Post-collision, Shoshonitic Volcanism on the Tibetan Plateau: Implications for Convective Thinning of the Lithosphere and the Source of Ocean Island Basalts. *J. Petrol.* **37**, 45–71.

Van Kooten G. K. (1980) Mineralogy, Petrology, and Geochemistry of an Ultrapotassic Basaltic Suite, Central Sierra Nevada, California, U.S.A. *J. Petrol.* **21**, 651–684.

van Westrenen W., Allan N. L., Blundy J. D., Purton J. A. and Wood B. J. (2000a) Atomistic simulation of trace element incorporation into garnets - comparison with experimental garnet-melt partitioning data. *Geochim. Cosmochim. Ac.* **64**, 1629–1639.

van Westrenen W., Blundy J. D. and Wood B. J. (2000b) Effect of Fe^{2+} on garnet-melt trace element partitioning: experiments in FCMAS and quantification of crystal-chemical controls in natural systems. *Lithos* **53**, 189–201.

Whitney D. L. and Evans B. W. (2010) Abbreviations for names of rock-forming minerals. *Am. Mineral.* **95**, 185–187.

Williams H. M., Turner S. P., Pearce J. A., Kelley S. P. and Harris N. B. W. (2004) Nature of the Source Regions for Post-collisional, Potassic Magmatism in Southern and Northern Tibet from Geochemical Variations and Inverse Trace Element Modelling. *J. Petrol.* **45**, 555–607.

Wilson S. A. (1997) Basalt, Columbia River, BCR-2. United States Geological Survey Certificate of Analysis.

Wood B. J. and Blundy J. (1997) A predictive model for rare earth element partitioning between clinopyroxene and anhydrous silicate melt. *Contrib. Mineral. Petr.* **129**, 166–181.

Workman R. K. and Hart S. R. (2005) Major and trace element composition of the depleted MORB mantle (DMM). *Earth Planet. Sc. Lett.* **231**, 53–72.

Yao L., Sun C. and Liang Y. (2012) A parameterized model for REE distribution between low-Ca pyroxene and basaltic melts with applications to REE partitioning in low-Ca pyroxene along a mantle adiabat and during pyroxenite-derived melt and peridotite interaction. *Contrib. Mineral. Petr.* **164**, 261–280.

Zanetti A., Mazzucchelli M., Rivalenti G. and Vannucci R. (1999) The Finero phlogopite-peridotite massif: an example of subduction-related metasomatism. *Contrib. Mineral. Petr.* **134**, 107–122.

Figure captions

Figure 1. Backscattered electron images of typical textures in trace element-enriched experiments at 1 and 3 GPa. Large circular holes (about 10 µm) are laser ablation pits. (a) Experiment tr06 (1 GPa, 1040 °C), with melt in equilibrium with phlogopite (Phl) and pargasite (Prg) and minor amounts of orthopyroxene (not shown) and olivine (not shown). (b) Experiment tr10 (3 GPa, 1250 °C), with interstitial quenched melt together with phlogopite, garnet (Grt), orthopyroxene (Opx) and clinopyroxene (Cpx). (c) Experiment tr10e (3 GPa, 1250 °C), with quenched melt in equilibrium with phlogopite, garnet, and clinopyroxene.

Figure 2. Experimental trace element partition coefficients between phlogopite and melt at 1 and 3 GPa. Elements are ordered along the *x*-axis according to their incompatibility during MORB formation (Hofmann, 1988). The shaded area indicates the range of mineral–melt partition coefficients determined in previous experimental studies (Guo and Green, 1990; Adam et al., 1993; LaTourette et al., 1995; Sweeney et al., 1995; Schmidt et al., 1999; Green et al., 2000; Adam and Green, 2006; Fabbrizio et al., 2010).

Figure 3. Experimental trace element partition coefficients between pargasite and melt at 1 GPa. Elements are ordered along the *x*-axis according to their incompatibility during MORB formation (Hofmann, 1988). The shaded area indicates the range of mineral–melt partition coefficients determined in previous experimental studies (Sweeney et al., 1992; Green et al., 1993; Dalpé and Baker, 1994; Brenan et al., 1995; LaTourette et al., 1995; Klein et al., 1997; Bottazzi et al., 1999; Adam and Green, 2006).

Figure 4. Lattice strain models applied to phlogopite-melt partition coefficients for tr07 (1 GPa, 1140 °C) experiment.

Figure 5. Lattice strain models applied to pargasite-melt partition coefficients for tr04 (1 GPa, 1040 °C) and sta19 (1 GPa, 1065 °C) experiments.

Figure 6. Lattice strain models applied to clinopyroxene-melt partition coefficients for tr07 (1 GPa, 1140 °C) and tr10e (3 GPa, 1250 °C) experiments.

Figure 7. Lattice strain models applied to orthopyroxene-melt partition coefficients for tr04 (1 GPa, 1040 °C) and tr10 (3 GPa, 1250 °C) experiments.

Figure 8. Phlogopite-melt partition coefficients for Ni, Ti, Sr, and Yb as a function of melt polymerization, expressed as NBO/T (Mysen 1983). The dashed gray vertical line corresponds to NBO/T = 0.49; at greater NBO/T values, melt structure does not significantly influence trace element partitioning (Gaetani 2004). Error bars are plotted at 2σ and are most often smaller than the symbol size.

Figure 9. Multi-element diagrams showing the results of forward batch melting models of fertile (top panels) and depleted (lower panels) phlogopite ±amphibole-bearing peridotites at 1 (left panels) and 3 GPa (right panels). The trace element concentrations of the primary melts are normalized to those of their sources to highlight inter-element fractionations and the efficacy of trace element transfer to the melt phase (all elements are incompatible with the bulk source lithology). The fertile peridotite is BriPhl, the starting material used in the experiments of Condamine and Médard (2014). At 1 GPa, BriPhl is a phlogopite + pargasite-bearing lherzolite with the modal mineralogy 58.2% Ol, 17.7% Opx, 10.0% Phl, 9.5% Cpx, 3.4% Prg, and 1.2% Spl (subsolidus assemblage of experiment sta10 in Condamine and Médard, 2014). At 3 GPa, pargasite is not stable and the modal mineralogy of BriPhl becomes 57.5% Ol, 15.5% Opx, 10.0% Phl, 8.5% Cpx, and 8.5% Grt (subsolidus assemblage of experiment 3LP-12 in Condamine et al., 2016). The depleted peridotite is HbzPhl, a phlogopite-bearing harzburgite with the modal mineralogy 62.5% Ol, 26.0% Opx, 10.0% Phl, and 1.5% Spl at 1 GPa (estimated from experiment hzb08 in Condamine and Médard, 2014) and 60.5% Ol, 22.0% Opx, 10.0% Phl, and 7.5% Grt at 3 GPa (subsolidus experiment 3LP-19 in Condamine et al., 2016). The modal abundance of each phase during non-modal batch melting was first calculated for each increment of 1 wt. % melt. BriPhl melting reactions at 1 GPa were implemented as: (1) 0.39 Phl + 0.49 Prg + 0.44 Opx + 0.11 Cpx = 0.49 Ol + 1 melt for 0–7 wt. % melt (i.e., until Prg exhaustion), followed by (2) 0.49 Phl + 0.56 Opx + 0.47 Cpx + 0.05 Spl = 0.58 Ol + 1 melt for 8–20 wt. % melt (nearing Phl exhaustion). At 3 GPa, the reaction is 0.59 Phl + 0.52 Cpx + 0.18 Grt = 0.06 Ol + 0.23 Opx + 1 melt for 0–16 wt. % melt. For HzbPhl, the 1 GPa melting reaction is 0.7 Phl + 1.24 Opx + 0.05 Spl = 0.99 Ol + 1 melt for 0–14% melt (i.e., until Phl is exhausted) and that at 3 GPa is 0.93 Phl + 0.46 Grt = 0.25 Ol + 0.14 Opx + 1 melt (for 0–10 wt. % melt). The partition coefficients used for phlogopite, amphibole, orthopyroxene, clinopyroxene, and garnet were the average values obtained in this study at each pressure. The Opx/melt partition coefficients for Rb and Ba at 3 GPa were arbitrarily set to 0.0001. Olivine partition coefficients for REEs are from McKenzie and O'Nions (1991), and those for Ti, Zr, Hf, Th, and U from Adam and Green (2006); averages of their

experiments at 1 and 2 GPa; LILEs (Rb, Ba, Sr) and Nb partition coefficients were set to 0.0001. Spinel partition coefficients were set to 0.0001. All retained values are reported in Table S1. The temperature necessary to generate each melt fraction was estimated based on the results of Condamine and Médard (2014) and Condamine et al. (2016). Mineral abbreviations from Whitney and Evans (2010).

Figure 10. Multi-element diagrams showing the influence of varied proportions of phlogopite in a lherzolite source at the onset of melting on the trace element concentrations of primary melts. The values were obtained running the same non-modal batch melting model displayed Figure 9 but with modified starting compositions computed as X% pure phlogopite and Y% herzolite component, the mode of which was 64.7% Ol, 19.7% Opx, 10.6% Cpx, 3.8% Prg, and 1.3% Spl.

Figure 11. Retrieving the trace element composition of the mantle source of post-collisional potassic rocks from the Variscan French Massif Central. The samples from the database compiled by Couzinié et al. (2016) were reported on a SiO_2–K_2O (a) and Ni vs. Mg# (b, calculated as MgO/FeOt+MgO) diagrams to identify primary mantle melt compositions, clarify the mineralogy of their mantle source (lherzolite vs. harzburgite, persistence of phlogopite in the residue) and the pressure at which melting took place. The trace element compositions of the source of two 'primitive' samples were back-calculated using the results of the model (Figure 9) and are depicted in the primitive mantle-normalised (after McDonough and Sun, 1995) multi element diagram (c). For sake of comparison, are also reported the compositions of: (i) a mixture of 15% global subducted sediment (Plank and Langmuir, 1998) + 85% Depleted Mantle (DM, Workman and Hart, 2005); (ii) a mixture of 15% average granulite-facies post-Archean terrains (Hacker et al., 2015) + 85% DM.

Table 1

Major and minor element compositions of starting materials (normalized to 100 wt. %).

	Phl[a]	Ol[a]	Opx[a]	Cpx[a]	Spl[a]	Bri5[b]	BriPhl	Lhz1050	Lhz1075	Lhz1150	3Lhz1250
n	13	12	12	7	18	4					
SiO_2	40.89	40.87	55.59	52.03	0.06	45.01	44.60	58.06	56.96	53.15	46.56
TiO_2	1.91	-	0.13	0.67	0.16	0.11	0.29	0.47	1.16	1.01	2.09
Al_2O_3	14.01	-	4.05	6.96	57.93	3.15	4.23	20.09	18.11	18.83	12.72
Cr_2O_3	1.00	-	0.29	0.79	9.28	0.34	0.41	-	-	-	-
FeO	2.67	9.94	6.40	2.94	11.79	7.81	7.29	1.66	1.31	3.74	7.34
MnO	-	0.13	0.13	-	-	0.13	0.12	-	-	-	-
MgO	24.55	48.59	32.67	14.87	20.78	40.57	38.97	2.43	3.56	6.30	12.25
CaO	-	0.07	0.64	19.92	-	2.68	2.41	4.13	3.60	8.59	8.12
Na_2O	0.92	-	0.11	1.83	-	0.21	0.28	4.59	6.65	1.81	2.84
K_2O	9.42	-	-	-	-	-	0.94	4.48	3.66	3.82	5.02
NiO	-	0.41	-	-	-	-	-	-	-	-	-
F	0.71	-	-	-	-	-	0.07	-	-	-	-
H_2O	3.93[c]	-	-	-	-	-	0.39	4.08	4.99	2.75	3.06
		-	-	-	-						
Mg#	94.2	89.7	90.1	90.0	75.9	90.3	90.5	72.2	82.9	75.0	74.8

n is the number of analyses. BriPhl is the phlogopite-lherzolite starting material. Lhz1050, Lhz1075, Lhz1150 and 3Lhz1250 are the melt compositions added to the phlogopite-lherzolite. See Table 2 for melt fractions added in each experiment.

[a]Phl was separated from the Finero metasomatized harzburgite. Ol, Opx, Cpx and Spl analyses of Bri5 xenolith. All minerals were analyzed by EPMA, normalized to 100 wt. %.

[b]Whole rock composition of Bri5 lherzolite xenolith, analyzed by ICP-AES at the Service d'Analyses des Roches et Minéraux (CRPG, Nancy).

[c]Calculated by stoichiometry.

1

2

3

4 **Table 2**

Run conditions and experimental modes.

| Run | T (°C) | t (h) | Melt added (wt. %) | Run product modes (wt. %) | | | | | | | | ΔFeO[1] | ΔH$_2$O[1] | NBO/T |
				Melt	Ol	Opx	Cpx	Grt	Phl	Prg	r²			
1 GPa experiments														
sta16	1040	95	Lhz1075 (55)	34.1 (18)	-	25.1 (19)	-	-	17 (3)	24 (4)	0.57	-1.9	-1.5	0.11
tr04	1040	117	Lhz1050 (72)	61.5 (5)	-	16.2 (6)	-	-	13.1 (9)	9.2 (11)	0.15	-9.7	-0.5	0.17
tr06	1040	145	Lhz1050 (76)	66.6 (17)	2.6 (20)	5.0 (26)	-	-	9.7 (12)	16.2 (9)	0.12	-8.2	-2.2	0.12
tr08	1040	145	Lhz1050 (76)	63.7 (7)	+	7.1 (9)	-	-	12.6 (13)	16.6 (16)	0.27	-8.7	-3.6	0.13
sta12[2]	1050	61	Lhz1075 (20)	13.8 (17)	34.8 (21)	19.8 (24)	3.6 (11)	-	19.5 (10)	8.5 (21)	0.20	-1.9	-1.5	0.16
sta19	1065	89	Lhz1075 (41)	56.7 (15)	-	11.2 (16)	-	-	20.0 (22)	12 (3)	0.95	-4.0	-1.5	0.22
tr07	1140	80	Lhz1150 (78)	61.6 (13)	-	12.0 (13)	11.0 (13)	-	15.4 (17)	-	0.43	-2.0	-0.6	0.35
3 GPa experiments														
tr09	1250	89	3Lhz1250 (75)	29 (4)	+	10.0 (23)	26 (3)	-	36 (3)	-	1.03	-4.8	-1.0	0.93
tr10	1250	89	3Lhz1250 (90)	27 (3)	-	7.7 (10)	12.3 (26)	8.0 (22)	44.9 (28)	-	0.73	-0.2	-0.2	0.96
tr09e	1250	89	3Lhz1250 (100)	59.5 (29)	-	-	20.2 (20)	-	20.3 (20)	-	1.19	-2.5	-1.0	0.76
tr10e	1250	89	3Lhz1250 (78)	57.6 (20)	-	-	7.9 (15)	26.6 (16)	7.9 (18)	-	0.83	-17.2	5.7	0.76

The numbers in parenthesis are 2σ standard deviations, given in the term of the last unit cited. r² is the sum of weighted squared residual from mass balance calculation. The experimental modes were obtained by mass balance calculations. Experiments tr09e and tr10e correspond to outer capsules of tr09 and tr10 experiments, respectively. Olivine is sometimes found as a minor phase (+). The 'Melt added' column corresponds to the proportion of synthetic melt inserted in the capsule, as well as its nature in parenthesis (see Table 1).

[1]FeO and H$_2$O relative gains (+) or losses (-) determined by mass balance calculations and expressed in %.

[2]Undoped experiment, re-analyzed from Condamine and Médard (2014).

5

Table 3

Melt and mineral major element compositions (wt. %) in experiments, determined by EMPA.

Run	T (°C)	Phase	n	SiO_2	TiO_2	Al_2O_3	Cr_2O_3	FeO	MnO	MgO	CaO	Na_2O	K_2O	NiO	H_2O	H_2O*	Sum
1 GPa experiments																	
sta16	1040	melt	8	58.1 (3)	1.32 (10)	18.18 (17)	0.56 (9)	1.98 (13)	-	2.15 (7)	1.73 (11)	5.80 (20)	4.21 (21)	-	5.95 (27)	-	93.42
		phl	6	39.3 (4)	4.6 (8)	15.6 (5)	0.14 (8)	4.5 (6)	-	21.7 (6)	-	1.30 (8)	8.78 (26)	-	4.3 (6)	-	93.50
		prg	4	44.5 (8)	2.2 (5)	12.7 (7)	0.12 (4)	6.45 (26)	-	17.6 (3)	9.67 (23)	3.84 (15)	0.81 (7)	-	2.1 (5)	-	94.41
		opx	3	56.7 (8)	0.43 (6)	3.6 (5)	0.15 (5)	2.0 (4)	-	36.8 (4)	0.25 (6)	0.11 (3)	-	-	-	-	99.01
tr04	1040	melt	13	59.5 (3)	0.35 (6)	18.57 (18)	0.17 (6)	2.32 (14)	-	3.33 (13)	3.95 (12)	4.72 (20)	3.33 (17)	-	3.75 (10)	7.64 (20)	92.65
		phl	8	38.97 (27)	1.24 (9)	16.98 (17)	-	5.79 (22)	0.11 (6)	22.21 (28)	-	1.16 (9)	9.00 (29)	0.32 (9)	4.2 (6)	-	94.23
		prg	6	43.1 (3)	0.81 (8)	13.63 (15)	-	6.82 (24)	-	18.05 (21)	11.44 (19)	2.62 (13)	1.23 (11)	0.18 (8)	2.1 (5)	-	96.26
		opx	5	54.8 (4)	0.10 (4)	5.23 (24)	0.07 (4)	3.36 (13)	-	35.5 (3)	0.86 (11)	-	-	0.12 (6)	-	-	99.55
tr06	1040	melt	33	60.89 (27)	0.26 (6)	18.56 (19)	-	1.44 (12)	-	2.20 (7)	3.33 (14)	4.91 (18)	4.55 (20)	-	3.86 (15)	5.3 (3)	92.89
		phl	16	39.4 (10)	1.80 (21)	17.1 (13)	0.21 (4)	4.2 (6)	-	22.4 (10)	-	0.93 (10)	9.55 (29)	0.16 (8)	4.3 (12)	-	93.87
		prg	13	43.8 (20)	1.08 (17)	14.3 (7)	0.25 (7)	5.1 (5)	-	18.2 (19)	11.3 (9)	2.57 (28)	1.4 (4)	-	2.1 (5)	-	95.78
		ol	3	42.0 (3)	-	-	-	6.8 (13)	0.14 (5)	50.7 (10)	0.05 (3)	-	-	0.38 (7)	-	-	99.77
		opx	18	55.9 (5)	0.11 (5)	4.0 (6)	0.18 (10)	6.0 (9)	0.20 (4)	32.4 (9)	0.83 (17)	0.09 (5)	-	0.12 (6)	-	-	100.47
tr08	1040	melt	14	61.1 (3)	0.39 (6)	18.39 (17)	-	1.84 (13)	-	2.55 (8)	3.62 (11)	4.60 (17)	3.92 (18)	-	3.6 (5)	5.1 (4)	90.54
		phl	5	40.5 (5)	2.07 (11)	16.88 (27)	0.26 (7)	4.41 (19)	-	21.2 (11)	0.20 (11)	1.16 (14)	8.91 (28)	0.16 (8)	4.3 (13)	-	91.78
		prg	6	44.0 (3)	1.14 (9)	14.0 (6)	0.30 (10)	5.57 (22)	-	18.0 (4)	10.85 (29)	2.75 (15)	1.40 (11)	-	2.1 (7)	-	93.54
		opx	6	55.62 (29)	0.13 (4)	4.5 (5)	0.28 (6)	5.7 (6)	0.11 (5)	32.53 (26)	0.76 (12)	0.15 (5)	-	0.09 (5)	-	-	98.89
sta12[1]	1050	melt	15	58.69 (21)	0.84 (8)	18.94 (13)	-	1.52 (8)	-	3.08 (10)	3.90 (17)	5.50 (11)	3.41 (12)	-	4.1 (6)	5.27 (18)	92.06
		phl	8	39.2 (5)	3.73 (20)	16.5 (6)	0.74 (12)	2.47 (6)	-	22.69 (28)	-	1.18 (9)	8.94 (17)	-	4.1 (7)	-	95.28
		prg	5	44.84 (11)	2.99 (23)	12.47 (17)	1.25 (14)	2.40 (9)	-	18.9 (4)	11.1 (3)	2.76 (5)	1.15 (4)	-	2.13 (29)	-	97.34
		ol	5	41.25 (17)	-	-	-	8.59 (21)	0.14 (4)	49.9 (3)	0.15 (3)	-	-	-	-	-	99.63
		opx	5	55.28 (28)	0.17 (1)	4.10 (20)	0.34 (5)	6.30 (10)	0.14 (5)	32.61 (9)	0.85 (9)	0.09 (3)	-	0.12 (3)	-	-	100.25
		cpx	5	52.14 (24)	0.63 (5)	6.45 (26)	0.69 (8)	3.31 (13)	0.09 (3)	15.27 (24)	19.68 (26)	1.64 (15)	-	0.08 (1)	-	-	99.99
sta19	1065	melt	11	57.15 (26)	1.06 (8)	17.22 (17)	0.26 (7)	2.39 (15)	-	3.27 (9)	2.71 (13)	7.36 (21)	3.12 (16)	-	5.5 (7)	-	89.74
		phl	5	39.3 (4)	4.6 (8)	15.6 (5)	0.14 (8)	4.5 (6)	-	21.7 (6)	-	1.30 (8)	8.78 (26)	-	4.3 (6)	-	93.50

		Phase	n														Sum
		prg	5	46.27 (19)	1.93 (15)	10.05 (18)	-	4.71 (15)	-	20.01 (19)	10.46 (19)	3.49 (11)	0.95 (7)	-	2.1 (3)	-	95.60
		opx	5	58.2 (6)	0.16 (5)	1.5 (3)	-	1.24 (23)	-	38.0 (5)	0.85 (6)	0.09 (4)	-	-	-	-	98.78
tr07	1140	melt	27	53.7 (5)	1.11 (9)	18.85 (25)	-	3.86 (18)	-	5.45 (12)	7.47 (22)	2.58 (13)	4.08 (19)	-	2.90 (19)	4.30 (15)	92.33
		phl	5	38.73 (19)	3.14 (15)	16.76 (17)	0.59 (9)	4.88 (20)	-	20.97 (29)	0.13 (10)	0.48 (7)	9.9 (3)	0.15 (8)	4.22 (16)	-	94.30
		opx	14	54.0 (5)	0.22 (4)	6.3 (6)	0.34 (11)	5.71 (20)	-	32.2 (4)	1.15 (8)	0.05 (3)	-	-	-	-	99.67
		cpx	8	49.71 (16)	0.78 (6)	7.6 (4)	0.28 (6)	4.39 (21)	-	15.5 (4)	21.12 (29)	0.49 (5)	-	-	-	-	99.40
3 GPa experiments																	
tr09	1250	melt	31	47.2 (4)	2.81 (12)	12.29 (15)	-	9.27 (27)	-	10.86 (27)	7.10 (23)	3.12 (16)	3.86 (18)	-	3.5 (10)	-	86.89
		phl	17	40.1 (3)	2.02 (11)	14.98 (18)	0.28 (10)	6.16 (23)	-	21.47 (28)	-	0.38 (6)	10.3 (3)	-	4.2 (8)	-	93.84
		opx	7	55.26 (24)	0.20 (4)	4.45 (18)	0.22 (6)	5.77 (16)	-	32.65 (22)	1.20 (5)	0.25 (4)	-	-	-	-	100.25
		cpx	15	52.5 (4)	0.46 (5)	5.84 (12)	0.26 (7)	5.91 (17)	-	16.29 (24)	16.60 (21)	2.10 (9)	0.06 (3)	-	-	-	98.72
tr10	1250	melt	6	47.17 (29)	2.53 (12)	12.48 (14)	-	8.8 (4)	-	11.3 (6)	7.94 (22)	2.92 (28)	3.9 (4)	-	3.1 (8)	-	88.49
		phl	7	40.60 (25)	1.80 (9)	15.17 (14)	0.29 (9)	4.53 (17)	-	22.63 (24)	-	0.34 (6)	10.4 (3)	-	4.2 (8)	-	94.20
		opx	6	56.02 (28)	0.15 (4)	3.25 (6)	0.21 (5)	7.04 (18)	-	31.85 (23)	1.30 (7)	0.18 (3)	-	-	-	-	99.83
		cpx	7	54.2 (3)	0.34 (6)	4.43 (20)	0.23 (5)	4.18 (13)	-	17.8 (3)	17.41 (26)	1.40 (11)	0.05 (3)	-	-	-	99.28
		grt	5	42.17 (23)	0.28 (4)	22.77 (26)	0.75 (12)	8.20 (19)	0.08 (4)	20.38 (20)	5.29 (14)	0.07 (3)	-	-	-	-	98.05
tr09e	1250	melt	9	48.69 (25)	2.69 (12)	13.29 (18)	-	8.11 (25)	-	8.33 (15)	6.97 (14)	2.99 (14)	5.29 (21)	-	3.7 (3)	-	87.39
		phl	8	40.3 (3)	2.35 (12)	15.24 (23)	-	6.34 (23)	-	21.09 (24)	-	0.27 (5)	10.2 (3)	-	4.2 (8)	-	93.92
		cpx	6	52.05 (21)	0.49 (5)	6.39 (13)	-	5.84 (16)	-	15.19 (29)	18.11 (18)	1.93 (9)	-	-	-	-	99.09
tr10e	1250	melt	4	49.0 (4)	2.45 (12)	13.4 (3)	-	6.74 (23)	-	9.28 (15)	7.27 (21)	2.59 (13)	5.51 (22)	-	3.8 (6)	-	86.46
		phl	3	40.47 (27)	2.67 (13)	15.20 (16)	-	4.55 (20)	-	22.01 (24)	-	0.26 (5)	10.6 (3)	-	4.2 (4)	-	94.21
		cpx	4	54.1 (3)	0.34 (6)	4.7 (6)	-	4.82 (16)	0.08 (4)	18.2 (5)	16.3 (6)	1.52 (10)	-	-	-	-	98.84
		grt	5	42.02 (23)	0.28 (4)	23.14 (16)	0.24 (11)	8.8 (4)	0.14 (5)	20.01 (29)	5.25 (26)	0.08 (3)	-	-	-	-	99.49

n is the number of EMPA analyses. The numbers in parenthesis are 2σ standard deviations, given in term of the last unit cited. Sum corresponds to the original EMPA analytical total. Phlogopite and pargasit contents have been estimated by structural formula calculations (Leake et al., 1997; Rieder et al., 1998). H_2O contents in melts have been estimated by mass balance calculations.

[1]Undoped experiment, re-analyzed from Condamine and Médard (2014).

*H_2O content determined by Raman spectroscopy.

Table 4

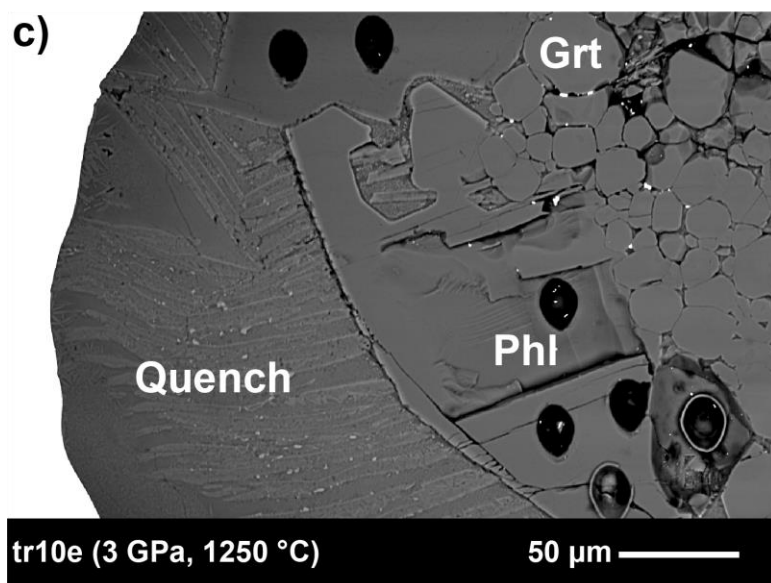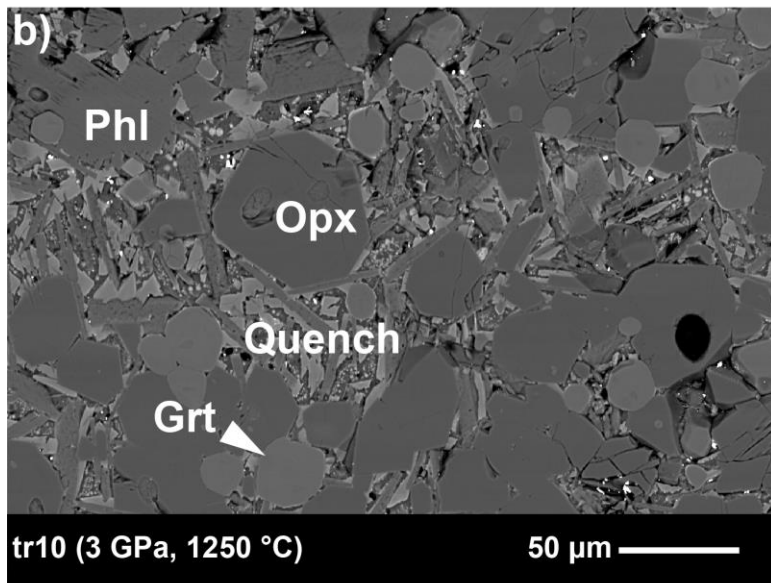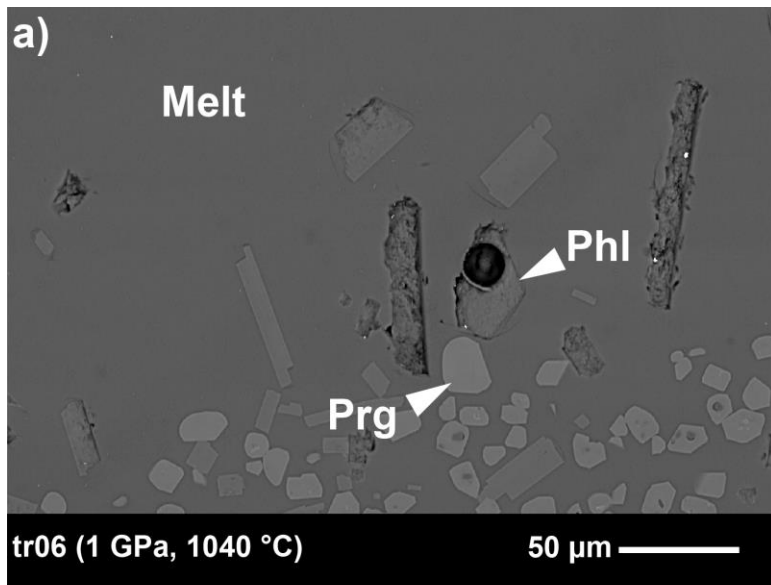Partition coefficients between minerals and melt ($D^{min/melt}$)

	sta16		tr04						tr06					
Run														
P (GPa)	1		1						1					
T (°C)	1040		1040						1040					
Phase	Phl		Phl		Prg		Opx		Phl		Prg		Opx	
	$D^{phl/melt}$	2 σ	$D^{phl/melt}$	2 σ	$D^{amp/melt}$	2 σ	$D^{opx/melt}$	2 σ	$D^{phl/melt}$	2 σ	$D^{amp/melt}$	2 σ	$D^{opx/melt}$	2 σ
Li^{7}	0.248	0.162	0.137	0.018	0.152	0.020	0.188	0.039	0.158	0.005	0.140	0.012	0.039	0.004
Be^{9}											0.274	0.029		
Ca^{44}	0.055	0.030			2.632	0.171	0.151	0.026	0.021	0.005	3.058	0.194	0.240	0.025
Sc^{45}	1.381	0.293	0.869	0.100	3.759	0.322	1.873	0.297	1.553	0.118	6.901	0.642	0.149	0.018
Ti^{47}			3.396	0.182	1.988	0.116	0.200	0.115	6.811	0.512	3.766	0.281	0.660	0.056
V^{51}	0.069	0.017	0.020	0.006	0.036	0.008	0.018	0.024	0.238	0.016	0.185	0.008	0.172	0.014
Cr^{53}	0.398	1.102	0.358	0.039	0.435	0.046	0.184	0.173						
Mn^{55}	6.302	7.069	8.339	0.608	5.389	0.445	3.479	0.454	0.536	0.110	1.177	0.099	12.347	1.230
Co^{59}	6.477	1.646	4.863	0.437	4.588	0.364	5.572	0.506	9.649	0.645	7.673	0.527	1.735	0.138
Ni^{60}	30.876	4.627	46.571	4.138	22.389	2.262	21.389	3.159	55.769	4.112	31.025	2.535	53.886	4.741
Rb^{85}	2.074	0.216	2.989	0.276	0.070	0.010	0.015	0.102	2.036	0.137	0.047	0.003		
Sr^{88}	0.315	0.048	0.246	0.013	0.359	0.014	0.013	0.025	0.248	0.017	0.441	0.029	0.001	0.001
Y^{89}	0.037	0.006	0.007	0.003	1.967	0.127	0.099	0.018	0.010	0.001	2.860	0.194	0.007	0.001
Zr^{90}	0.057	0.008	0.047	0.006	0.309	0.027	0.031	0.010	0.054	0.004	0.404	0.020	0.003	0.001
Nb^{93}	0.337	0.050	0.255	0.020	0.336	0.025	0.016	0.009	0.442	0.019	0.585	0.038		
Ba^{137}	4.482	1.808	4.197	0.353	0.148	0.021	0.016	0.243	4.601	0.345	0.202	0.016		
La^{139}	0.027	0.005	0.002	0.002	0.215	0.015					0.276	0.013		
Ce^{140}	0.029	0.005	0.003	0.002	0.120	0.010	0.003	0.001			0.488	0.017		
Nd^{146}	0.033	0.008			0.937	0.034					1.328	0.062		
Sm^{147}	0.040	0.011			1.535	0.123	0.009	0.006			2.305	0.154		
Eu^{153}	0.037	0.008	0.004	0.003	1.812	0.123	0.020	0.003			2.791	0.185		
Gd^{157}	0.034	0.013			1.999	0.172	0.033	0.008			3.049	0.214		
Dy^{163}	0.035	0.010			2.141	0.147	0.074	0.008			3.366	0.231		
Ho^{165}	0.034	0.007	0.009	0.002	2.116	0.143	0.103	0.008			3.261	0.228	0.001	0.000
Yb^{172}	0.036	0.009	0.016	0.007	1.712	0.135	0.219	0.019			2.590	0.178		
Lu^{175}	0.041	0.007	0.017	0.002	1.547	0.108	0.256	0.018	0.013	0.002	2.176	0.146		
Hf^{178}	0.063	0.018	0.057	0.007	0.503	0.042	0.044	0.012	0.064	0.001	0.752	0.048		
Ta^{181}	0.183	0.045	0.237	0.019	0.324	0.025	0.015	0.005	0.352	0.022	0.507	0.009		
Th^{232}	0.027	0.006	0.008	0.001	0.035	0.003	0.011	0.004	0.007	0.001	0.048	0.004		
U^{238}	0.042	0.007	0.013	0.001	0.010	0.002	0.011	0.004	0.013	0.001	0.012	0.001		

tr08						sta12				sta19					
1						1				1					
1040						1050				1065					
Phl		Prg		Opx		Phl		Prg		Phl		Prg		Opx	
$D^{phl/melt}$	2 σ	$D^{amp/melt}$	2 σ	$D^{opx/melt}$	2 σ	$D^{phl/melt}$	2 σ	$D^{amp/melt}$	2 σ	$D^{phl/melt}$	2 σ	$D^{amp/melt}$	2 σ	$D^{opx/melt}$	2 σ
0.188	0.007	0.270	0.021	0.303	0.024	0.153	0.153	0.242	0.162	0.227	0.152	0.139	0.045	0.195	0.006
0.032	0.010	2.733	0.174	0.213	0.045	0.028	0.017	2.893	0.093	0.045	0.013	2.315	0.129	0.215	0.029
0.962	0.067	4.426	0.290	2.381	0.160	0.955	0.016	2.418	0.061	0.481	0.032	2.780	0.356	0.776	0.127
5.396	0.396	2.635	0.043	0.375	0.038										
0.521	0.003	0.429	0.027	0.102	0.008					0.031	0.004	0.011	0.003	0.026	0.006
										0.135	0.057	0.102	0.012	0.048	0.010
0.642	0.046	1.701	0.277	5.156	0.520	0.839	0.308	1.742	0.836	6.512	1.108	2.652	0.366	1.562	0.517
7.258	0.455	4.952	0.343	10.502	0.728	6.175	0.509	3.522	0.400	4.255	0.261	2.274	0.158	4.573	0.766
54.831	3.068	29.698	2.294	62.855	4.737	84.471	7.924	31.627	4.735	32.482	3.474	13.510	1.420	19.404	1.799
2.448	0.165	0.111	0.009	0.012	0.003	2.458	0.035	0.115	0.015	2.203	0.214	0.027	0.002	0.025	0.003
0.300	0.021	0.588	0.040	0.019	0.003	0.154	0.008	0.368	0.012	0.202	0.022	0.232	0.017	0.019	0.003
0.009	0.001	2.258	0.143	0.187	0.014					0.019	0.003	0.811	0.097	0.077	0.010
0.044	0.003	0.357	0.033	0.044	0.005	0.037	0.005	0.368	0.106	0.041	0.005	0.138	0.013	0.026	0.004
0.388	0.026	0.465	0.031	0.025	0.003	0.601	0.118	0.435	0.032	0.180	0.025	0.165	0.019	0.027	0.004
6.274	0.492	0.321	0.030	0.018	0.008	3.248	0.089	0.203	0.038	3.186	0.202	0.087	0.014	0.022	0.008
0.013	0.002	0.299	0.023	0.062	0.002					0.017	0.004	0.111	0.012	0.018	0.003
0.011	0.002	0.521	0.042	0.059	0.003					0.019	0.003	0.040	0.005	0.027	0.004
0.012	0.005	1.118	0.101	0.075	0.020					0.016	0.007	0.473	0.054	0.030	0.007
0.013	0.007	1.591	0.142	0.084	0.008					0.020	0.010	0.760	0.066	0.040	0.009
0.019	0.004	1.764	0.146	0.093	0.005					0.024	0.005	0.863	0.078	0.042	0.007
0.009	0.005	1.746	0.145	0.101	0.027					0.014	0.009	0.933	0.120	0.044	0.003
0.012	0.004	1.851	0.159	0.181	0.028					0.016	0.002	0.895	0.090	0.070	0.004
0.013	0.002	1.789	0.156	0.219	0.023					0.017	0.001	0.905	0.114	0.078	0.005
0.017	0.006	1.617	0.137	0.460	0.023					0.022	0.005	0.683	0.083	0.115	0.018
0.012	0.001	1.458	0.122	0.406	0.034					0.022	0.004	0.605	0.080	0.130	0.018
0.054	0.004	0.601	0.041	0.070	0.008					0.046	0.004	0.262	0.038	0.027	0.007
0.307	0.015	0.433	0.035	0.028	0.003					0.170	0.027	0.161	0.017	0.023	0.005
0.006	0.001	0.114	0.011	0.040	0.004					0.021	0.004	0.005	0.001	0.023	0.005
0.008	0.001	0.096	0.010	0.023	0.003					0.025	0.005			0.029	0.004

tr07						tr09						tr09e			
1						3						3			
1140						1250						1250			
Phl		Opx		Cpx		Phl		Opx		Cpx		Phl		Cpx	
$D^{phl/melt}$	2 σ	$D^{opx/melt}$	2 σ	$D^{cpx/melt}$	2 σ	$D^{phl/melt}$	2 σ	$D^{opx/melt}$	2 σ	$D^{cpx/melt}$	2 σ	$D^{phl/melt}$	2 σ	$D^{cpx/melt}$	2 σ
0.127	0.003	0.184	0.014	0.211	0.018	0.2262	0.0228					0.3107	0.0256	0.2779	0.0197
												0.0395	0.0029	0.1018	0.0072
0.011	0.008	0.134	0.017	3.078	0.401	0.0103	0.0037	0.1712	0.0042	2.1764	0.1359	0.0094	0.0010	2.1804	0.2005
0.451	0.033	1.208	0.078	2.894	0.186	0.1492	0.0081					0.1903	0.0060	1.2432	0.0694
2.596	0.247	0.181	0.017	0.669	0.039	0.7371	0.0144					0.8423	0.0754	0.1756	0.0157
0.960	0.063	0.134	0.009	0.350	0.023	0.1820	0.0079					0.1959	0.0145	0.0741	0.0049
						4.6404	0.4055					13.0880	2.3713	12.9670	2.3385
0.216	0.092	3.414	0.294	2.698	0.273	0.2101	0.0459					0.2138	0.0230	0.5597	0.0654
2.823	0.128	3.246	0.041	1.341	0.098	1.3384	0.0534	1.7614	0.1278	0.7834	0.0578	1.9228	0.1586	0.7337	0.0500
21.034	1.970	14.705	1.235	8.167	0.742	5.4424	0.3411					7.5302	0.7400	1.8528	0.1384
2.768	0.175	0.002	0.001			3.7368	0.3003					3.6285	0.7831	0.0074	0.0014
0.212	0.009	0.002	0.001	0.117	0.008	0.0623	0.0081					0.0811	0.0051	0.1259	0.0046
		0.085	0.006	1.038	0.073	0.0005	0.0002					0.0005	0.0001	0.3130	0.0213
0.044	0.004	0.025	0.002	0.220	0.016	0.0121	0.0007					0.0107	0.0008	0.0484	0.0043
0.298	0.023	0.001	0.001	0.010	0.002	0.0459	0.0032					0.0436	0.0030	0.0089	0.0008
3.527	0.294					1.7259	0.1307					1.5938	0.1140	0.0100	0.0010
0.001	0.000	0.013	0.002	0.113	0.008	0.0002	0.0001	0.0005	0.0002	0.0366	0.0024	0.0001	0.0000	0.0398	0.0026
0.001	0.000	0.014	0.000	0.210	0.014	0.0001	0.0000	0.0010	0.0001	0.0617	0.0049	0.0001	0.0000	0.0638	0.0043
0.003	0.003	0.017	0.002	0.481	0.034			0.0034	0.0007	0.1381	0.0123	0.0002	0.0001	0.1354	0.0083
		0.026	0.001	0.805	0.052	0.0008	0.0004	0.0078	0.0007	0.2272	0.0209	0.0001	0.0001	0.2157	0.0107
0.008	0.002	0.033	0.004	0.888	0.057	0.0007	0.0002	0.0116	0.0006	0.2706	0.0235	0.0006	0.0001	0.2546	0.0106
0.008	0.004	0.043	0.008	1.008	0.065	0.0011	0.0007	0.0135	0.0010	0.2804	0.0233	0.0002	0.0001	0.2804	0.0150
		0.080	0.008	1.146	0.073	0.0005	0.0004	0.0287	0.0027	0.3431	0.0294	0.0002	0.0000	0.3163	0.0156
0.001	0.001	0.103	0.006	1.143	0.070	0.0002	0.0001	0.0344	0.0021	0.3531	0.0332	0.0003	0.0000	0.3247	0.0159
0.003	0.002	0.189	0.011	0.993	0.062	0.0013	0.0006	0.0627	0.0055	0.3336	0.0276	0.0013	0.0001	0.2801	0.0168
0.005	0.001	0.174	0.012	0.839	0.059	0.0020	0.0003	0.0688	0.0033	0.3036	0.0261	0.0021	0.0002	0.2668	0.0174
0.050	0.004	0.040	0.003	0.359	0.025	0.0164	0.0013					0.0141	0.0013	0.0857	0.0081
0.260	0.020	0.002	0.001	0.030	0.003	0.0470	0.0041					0.0414	0.0034	0.0094	0.0006
		0.001	0.000	0.017	0.001	0.0001	0.0001					0.0000	0.0000	0.0086	0.0008
0.001	0.000	0.001	0.000	0.005	0.001	0.0006	0.0001					0.0006	0.0001	0.0090	0.0008

	tr10						tr10e					
		3							3			
		1250							1250			
Phl		Opx		Grt			Phl		Cpx		Grt	
$D^{phl/melt}$	2 σ	$D^{opx/melt}$	2 σ	$D^{grt/melt}$	2 σ		$D^{phl/melt}$	2 σ	$D^{cpx/melt}$	2 σ	$D^{grt/melt}$	2 σ
0.1947	0.0198	0.2288	0.0180	0.0662	0.0070		0.2798	0.0114	0.2909	0.0207	0.0612	0.0047
		0.1541	0.0144	0.6076	0.0399				2.1489	0.1988	0.6532	0.0559
0.1315	0.0033	0.3725	0.0185	3.1198	0.1942		0.1469	0.0109	1.0830	0.0992	3.5372	0.2657
0.7242	0.0211	0.0569	0.0029	0.1031	0.0059		1.0992	0.0751	0.1328	0.0102	0.1234	0.0135
0.9940	0.0303	0.3921	0.0117	0.7425	0.0323		1.5770	0.1000	1.3751	0.1143	1.0611	0.0882
5.4139	0.5813	5.3542	0.1939	18.4585	1.4242		5.8199	0.8182	5.8041	0.9007	15.1074	2.2625
0.1504	0.0341	0.8921	0.0634	1.9784	0.1394		0.1989	0.0188	1.0620	0.0881	2.5629	0.2060
1.3878	0.0913	1.5045	0.0385	1.0809	0.0708		1.8467	0.0718	0.9829	0.0697	1.4603	0.1014
7.0394	0.5262	6.0860	0.4177	0.7645	0.1323		7.7947	0.7764	1.9013	0.2820	0.5019	0.2187
4.0538	0.2593			0.0022	0.0007		2.9350	0.1861	0.0009	0.0003	0.0005	0.0001
0.0637	0.0014	0.0011	0.0002	0.0037	0.0005		0.0520	0.0034	0.0972	0.0095	0.0020	0.0003
0.0005	0.0002	0.0276	0.0011	1.8244	0.1228		0.0004	0.0000	0.2900	0.0246	1.8981	0.1588
0.0092	0.0006	0.0040	0.0002	0.0933	0.0062		0.0110	0.0011	0.0371	0.0037	0.0976	0.0093
0.0500	0.0023	0.0002	0.0000	0.0006	0.0002		0.0758	0.0069	0.0013	0.0003	0.0005	0.0002
1.2900	0.0491						1.0107	0.0559	0.0008	0.0005	0.0008	0.0006
0.0002	0.0001	0.0003	0.0001	0.0016	0.0002		0.0001	0.0001	0.0255	0.0023	0.0060	0.0011
0.0002	0.0001	0.0008	0.0001	0.0032	0.0003				0.0480	0.0043	0.0091	0.0013
0.0004	0.0004	0.0025	0.0004	0.0196	0.0015				0.1097	0.0102	0.0255	0.0033
0.0006	0.0001	0.0060	0.0007	0.1106	0.0010				0.1847	0.0163	0.1174	0.0113
0.0036	0.0004	0.0083	0.0006	0.2084	0.0036		0.0036	0.0004	0.2136	0.0190	0.2151	0.0195
		0.0107	0.0010	0.3688	0.0063				0.2449	0.0218	0.3899	0.0353
0.0004	0.0001	0.0211	0.0016	1.1799	0.0480				0.2872	0.0263	1.2394	0.1135
0.0003	0.0001	0.0273	0.0018	1.8901	0.0607		0.0003	0.0002	0.2932	0.0232	1.9395	0.1525
0.0011	0.0004	0.0489	0.0033	4.4825	0.2470		0.0012	0.0006	0.2579	0.0229	4.5528	0.3971
0.0016	0.0002	0.0531	0.0012	5.4930	0.3039		0.0015	0.0003	0.2413	0.0217	5.4268	0.4849
0.0122	0.0008	0.0070	0.0003	0.0780	0.0052		0.0140	0.0013	0.0683	0.0063	0.0792	0.0073
0.0517	0.0034	0.0003	0.0000	0.0008	0.0002		0.0725	0.0065	0.0021	0.0003	0.0008	0.0002
0.0001	0.0001	0.0001	0.0000	0.0003	0.0000		0.0001	0.0000	0.0019	0.0002	0.0003	0.0001
0.0002	0.0001	0.0001	0.0000	0.0014	0.0002		0.0003	0.0001	0.0019	0.0002	0.0017	0.0002
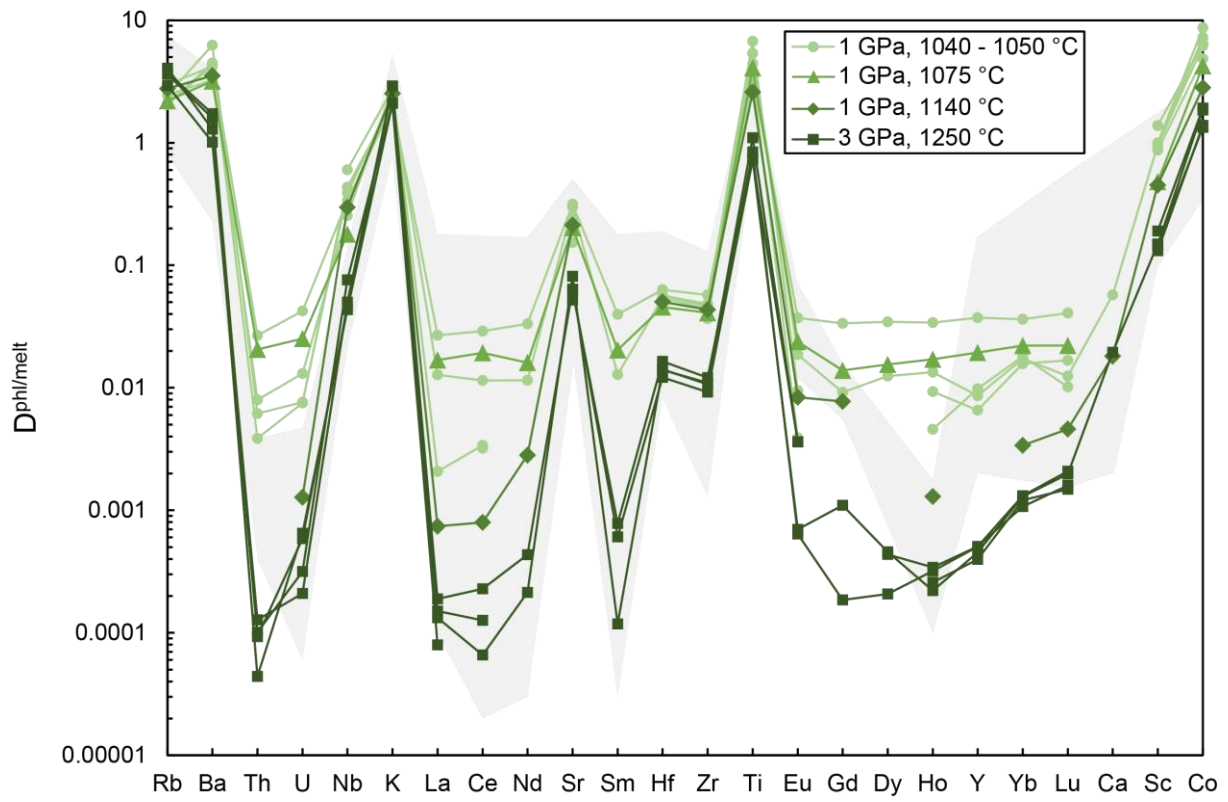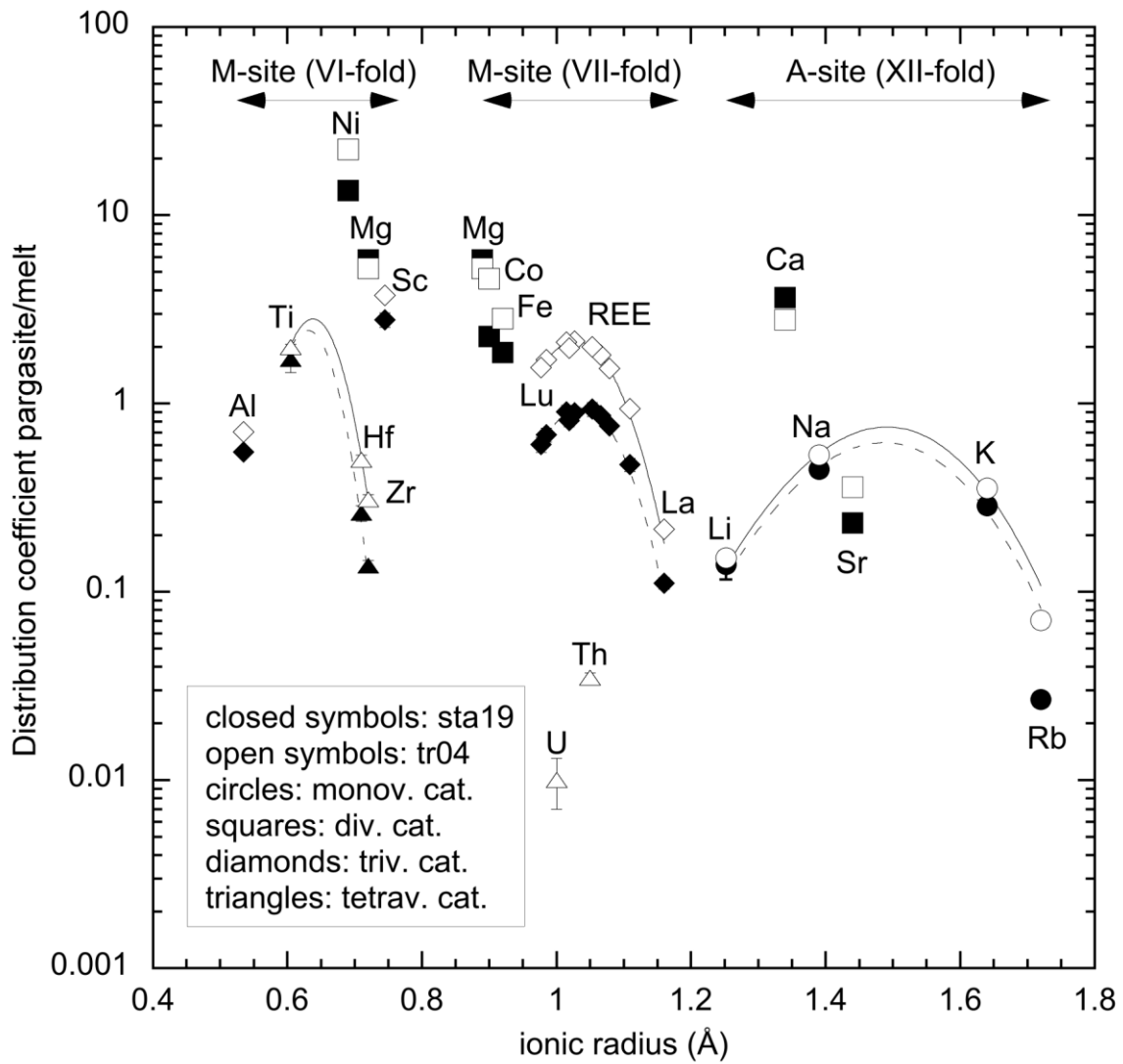
9

10

11 **Figure 1**

a) Melt — Phl — Prg — tr06 (1 GPa, 1040 °C) — 50 µm

b) Phl — Opx — Quench — Grt — tr10 (3 GPa, 1250 °C) — 50 µm
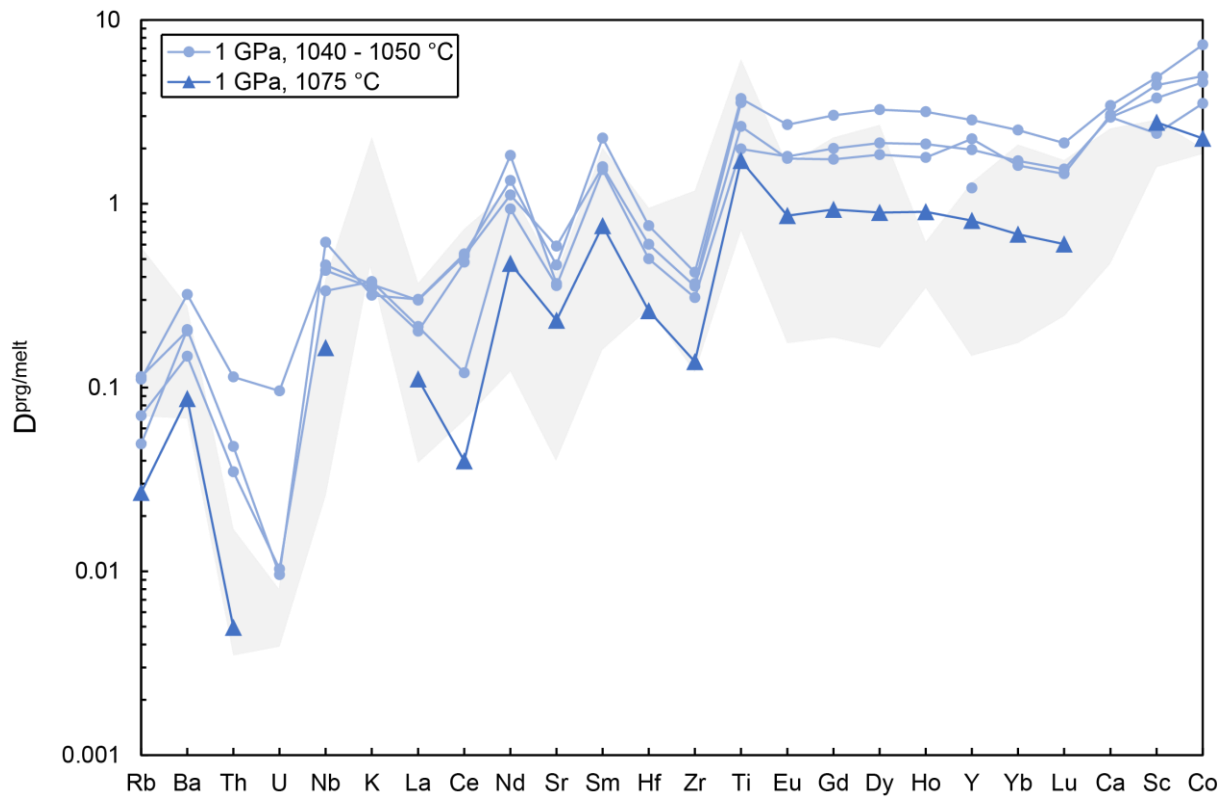
c) Grt — Quench — Phl — tr10e (3 GPa, 1250 °C) — 50 µm

12

13   **Figure 2**
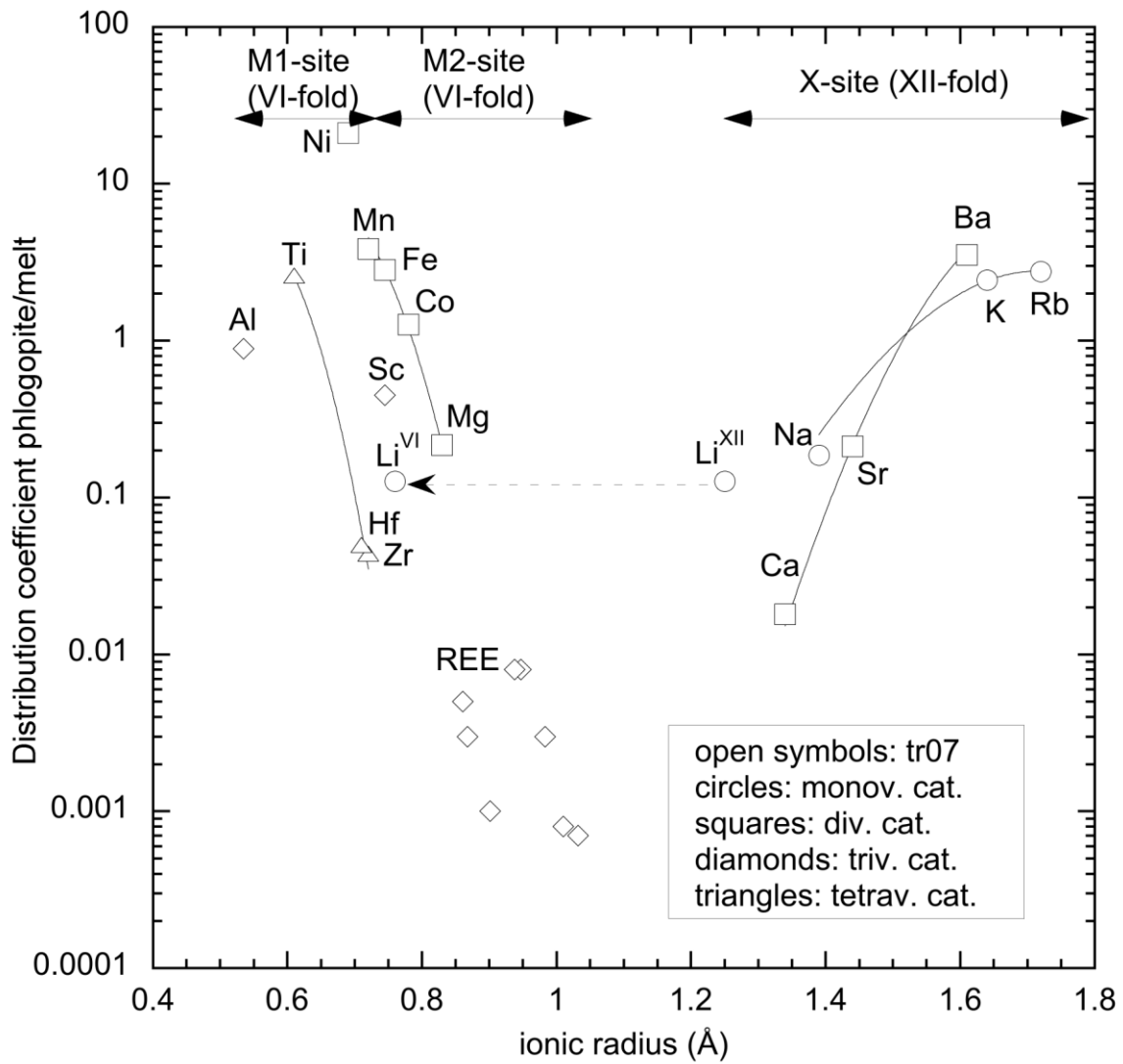
16   **Figure 3**

19 **Figure 4**

20

21

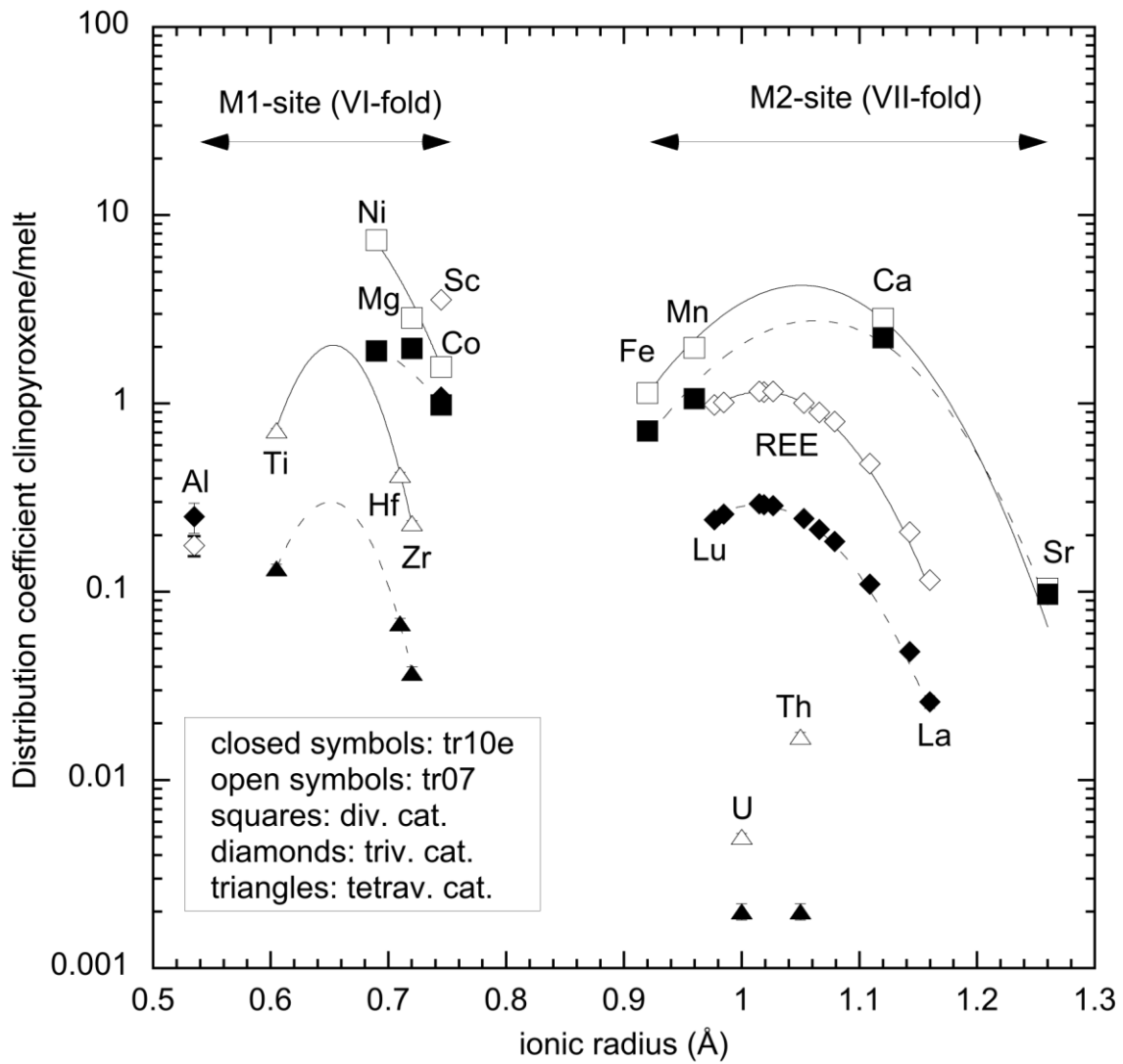**Figure 5**

Figure 6

28   **Figure 7**
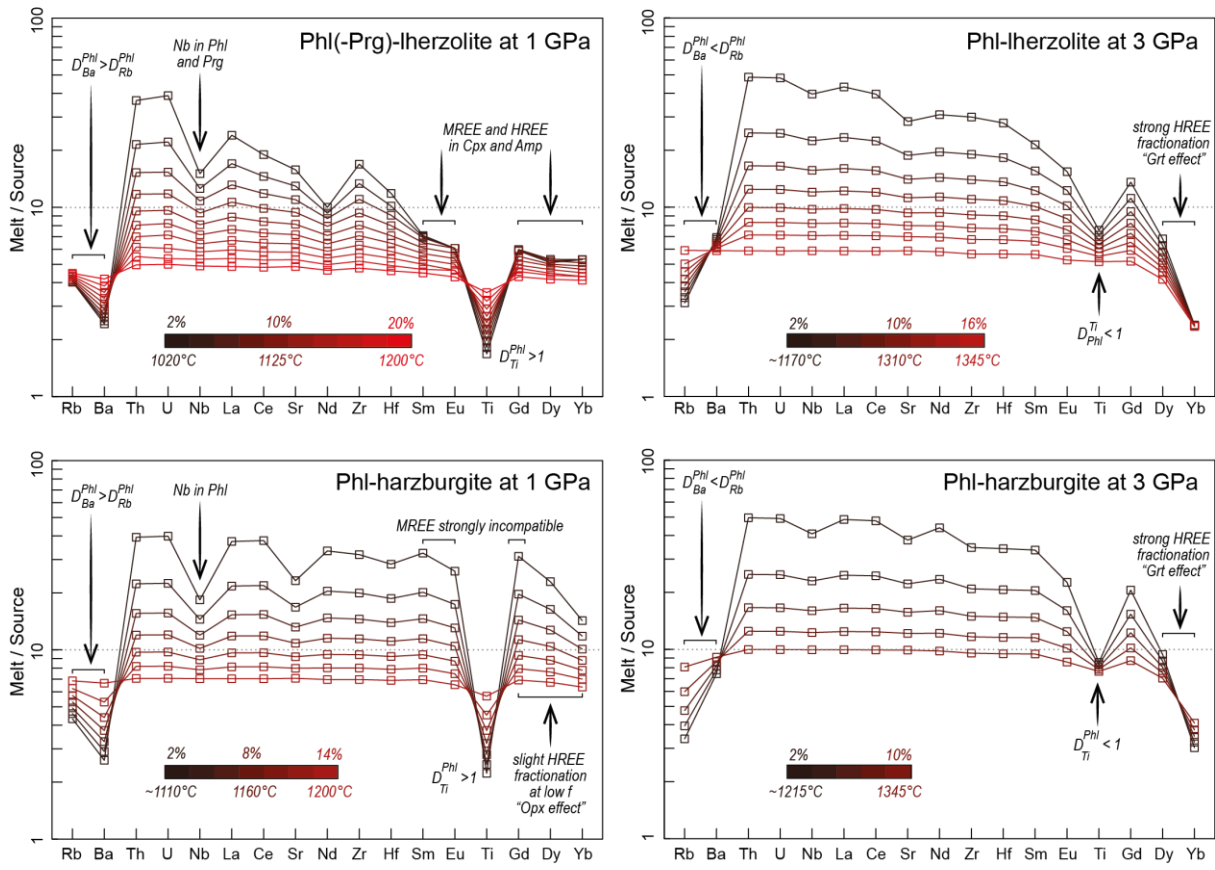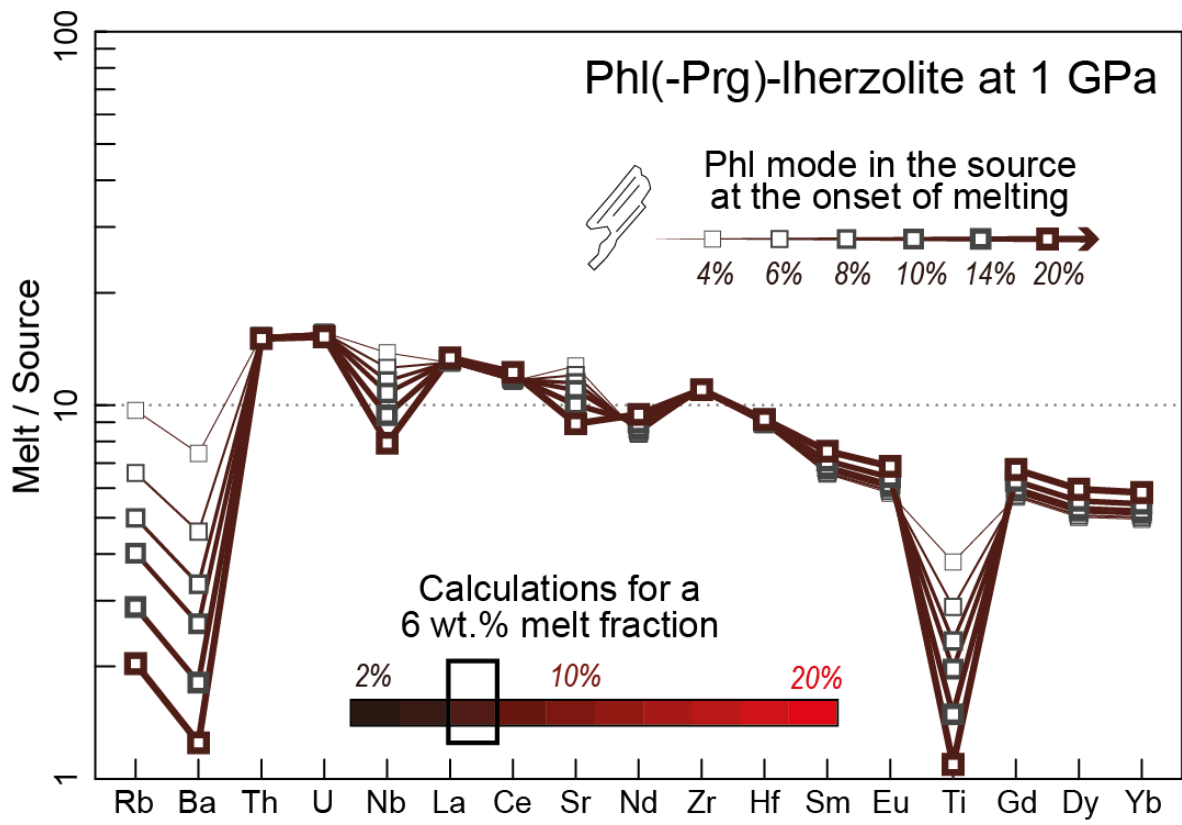
31 **Figure 8**

34   **Figure 9**

35

36
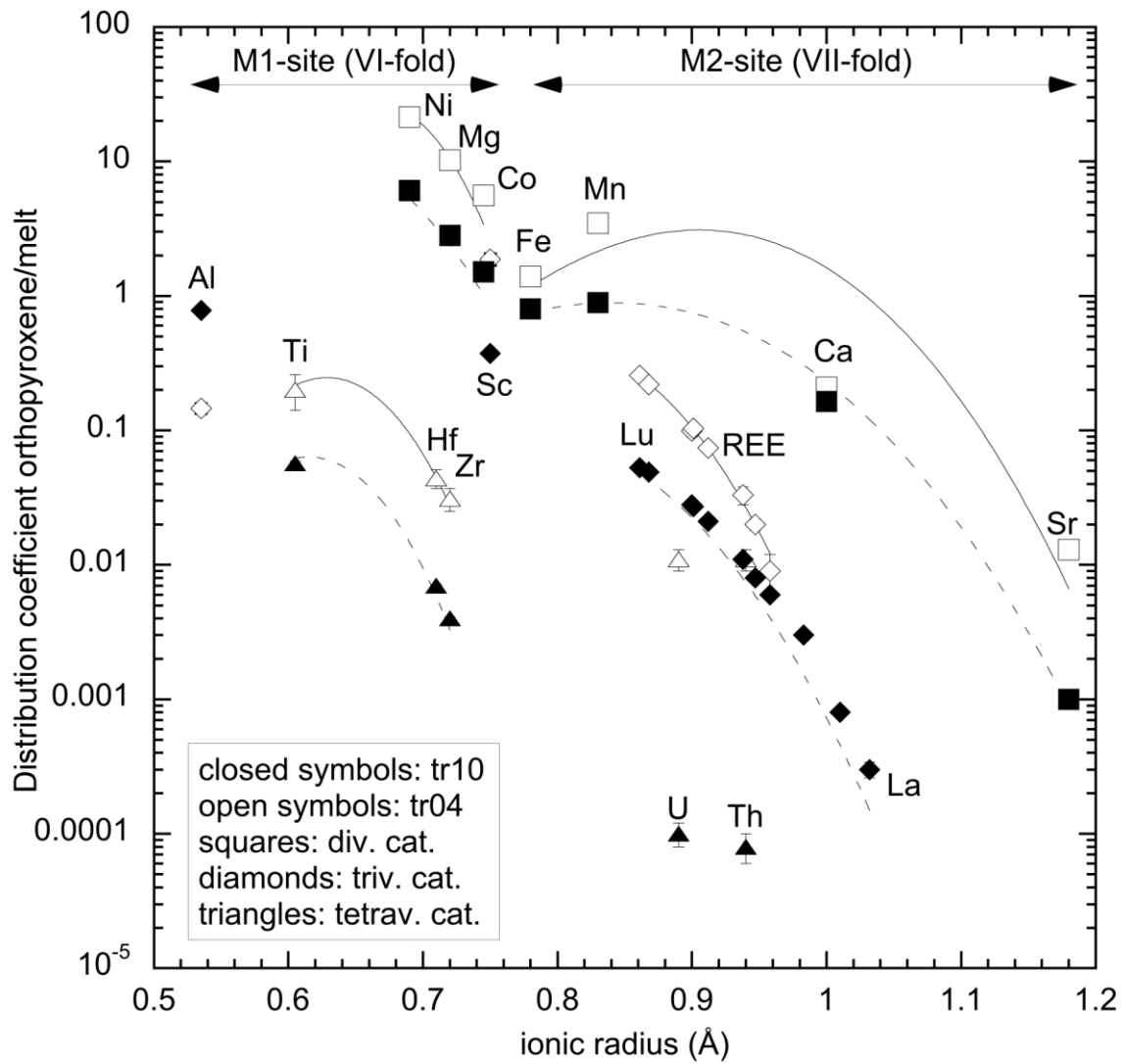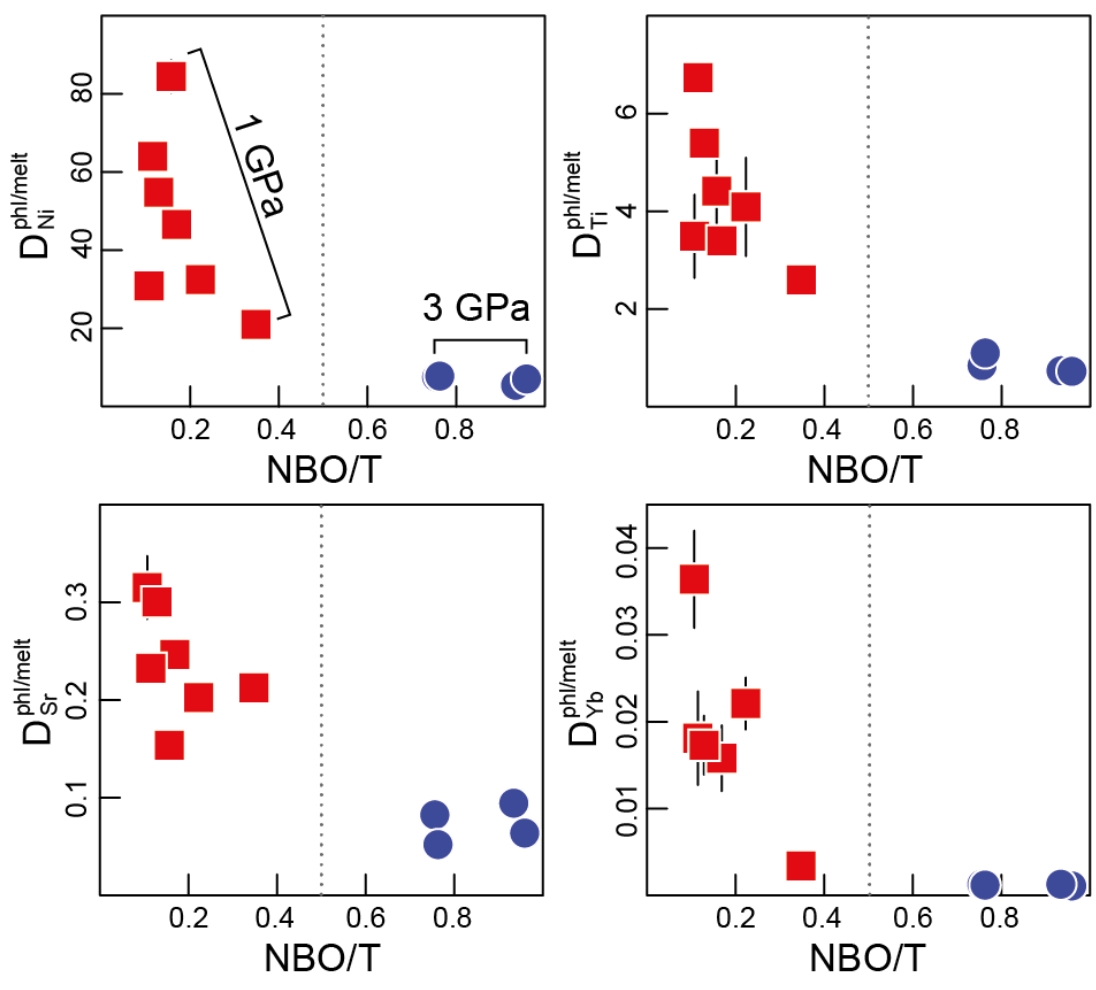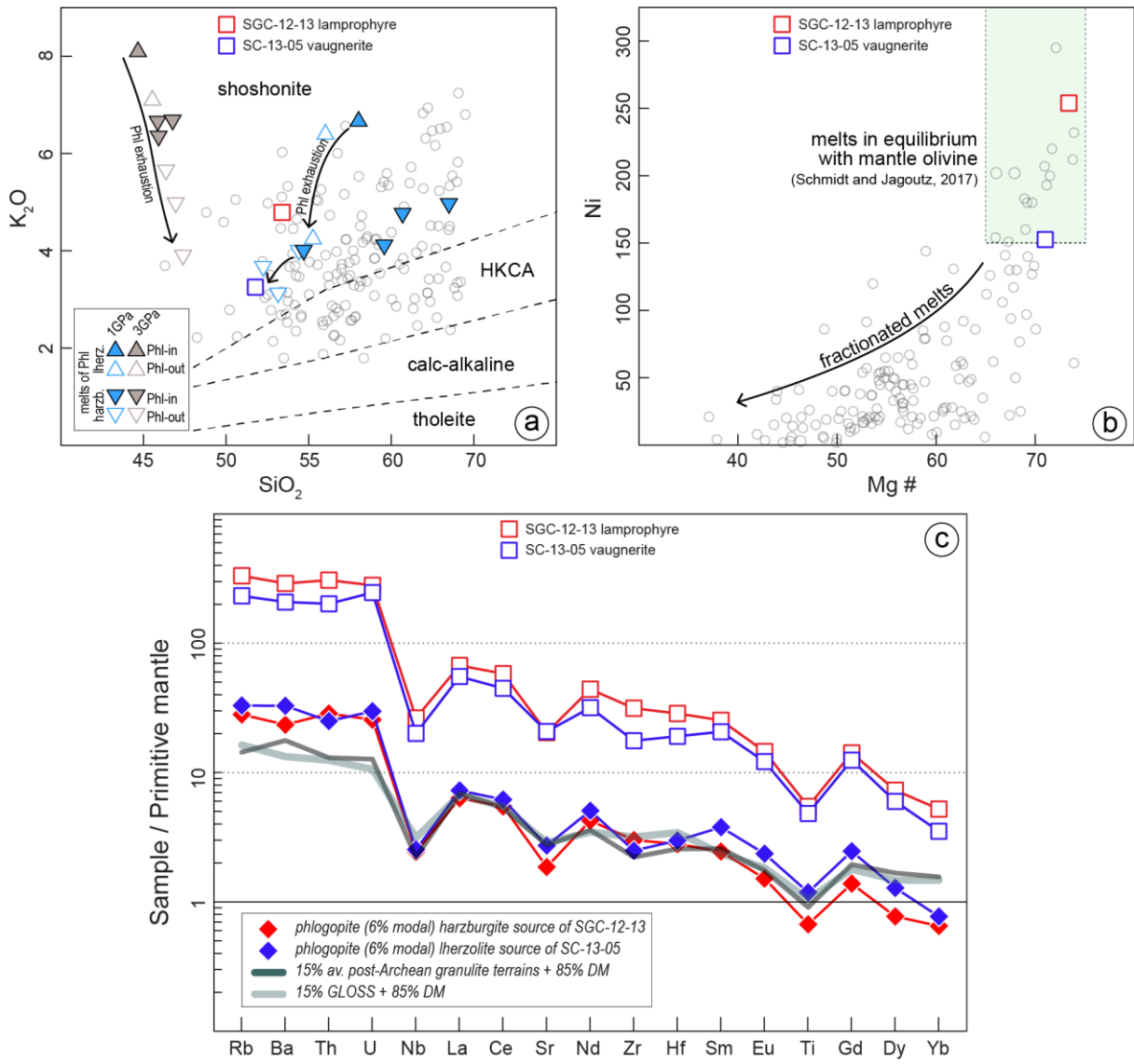
Figure 10

40   **Figure 11**

Supplementary Material

Trace element partitioning during incipient melting of phlogopite-peridotite in the spinel and garnet stability fields

P. Condamine, S. Couzinié, A. Fabbrizio, J.-L. Devidal, E. Médard

List of Supplementary Figures

58 **Figure S1.** Experimental trace element partition coefficients between mineral and melt for pyroxenes
59 and garnet. Elements are classified as a function of their incompatibility order during MORB
60 formation (Hofmann, 1988). The shaded area corresponds to the range of mineral – melt partition
61 coefficients determined in previous experimental studies: a) clinopyroxene (Hart and Dunn, 1993;
62 Blundy and Dalton, 2000; Green et al., 2000; McDade et al., 2003; Adam and Green, 2006; Tuff and
63 Gibson, 2007); b) orthopyroxene (Kennedy et al., 1993; Green et al., 2000; McDade et al., 2003;
64 Adam and Green, 2006; Klemme et al., 2006); c) garnet (Shimizu, 1980; Sweeney et al., 1992; Adam
65 and Green, 2006; Tuff and Gibson, 2007).
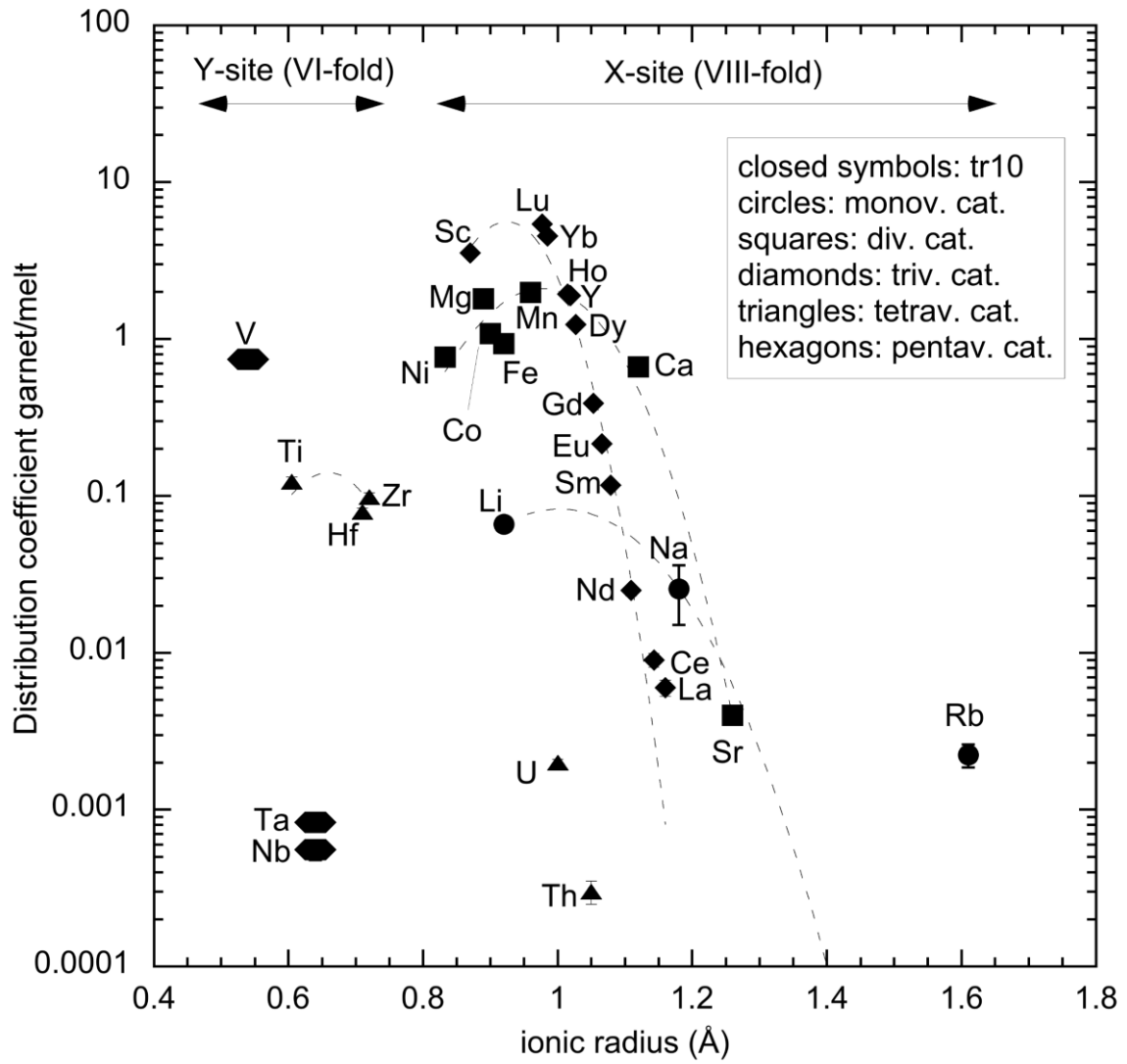
66 **Figure S2.** Lattice strain models applied to garnet-melt partition coefficients for tr10 (3 GPa, 1250 °C)
67 experiment.
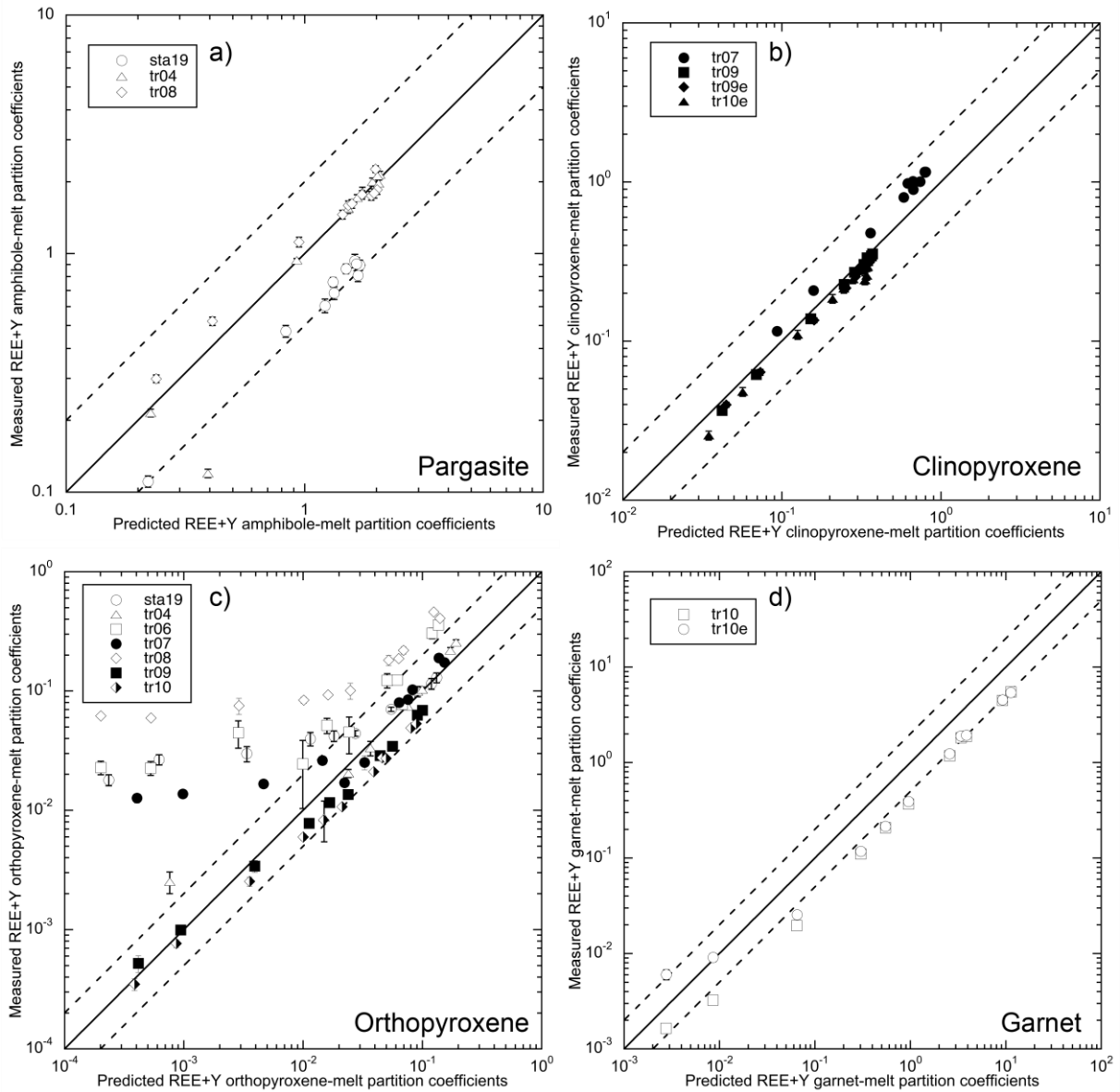
Figure S3. Measured REE+Y mineral – melt partition coefficients for: a) pargasitic amphibole plotted against those calculated using the model of Shimizu et al. (2017); b) clinopyroxene plotted against those calculated using the model of Sun and Liang (2012); c) orthopyroxene plotted against those calculated using the model of Yao et al. (2012); d) garnet plotted against those calculated using the model of Sun and Liang (2013, 2014). The solid lines are 1:1, dashed lines are 1:2 and 2:1.
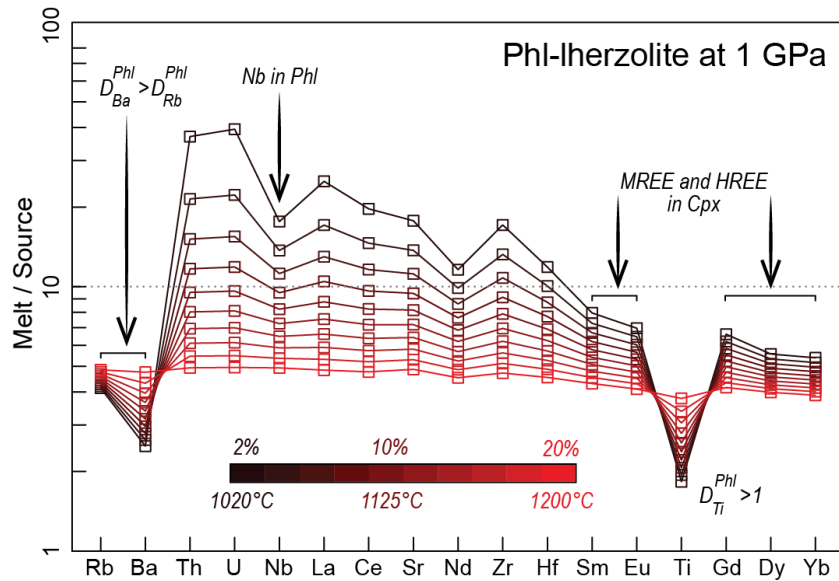
73 **Figure S4.** Multi-element diagram showing the results of a forward batch melting model of a fertile
74 phlogopite-bearing but pargasite-free peridotite at 1 GPa. The model is designed to test the
75 respective roles of clinopyroxene and pargasite in fractionating LREE from MREE and HREE. The
76 calculation parameters (melting reactions, partition coefficients) are identical to those described in
77 Figure 9 but the BriPhl source is modified to remove pargasite considering the reaction Cpx + Opx +
78 fluid = Prg + Ol (Condamine and Médard, 2014). The resulting phlogopite-bearing but pargasite-free
79 lherzolite has a mode 0.548 Ol, 0.211 Opx, 0.100 Phl, 0.129 Cpx and 0.012 Spl. The obtained pattern
80 does not substantially differ from that of the top left panel in Figure 9, demonstrating LREE/MREE
81 fractionation is primarily caused by clinopyroxene.
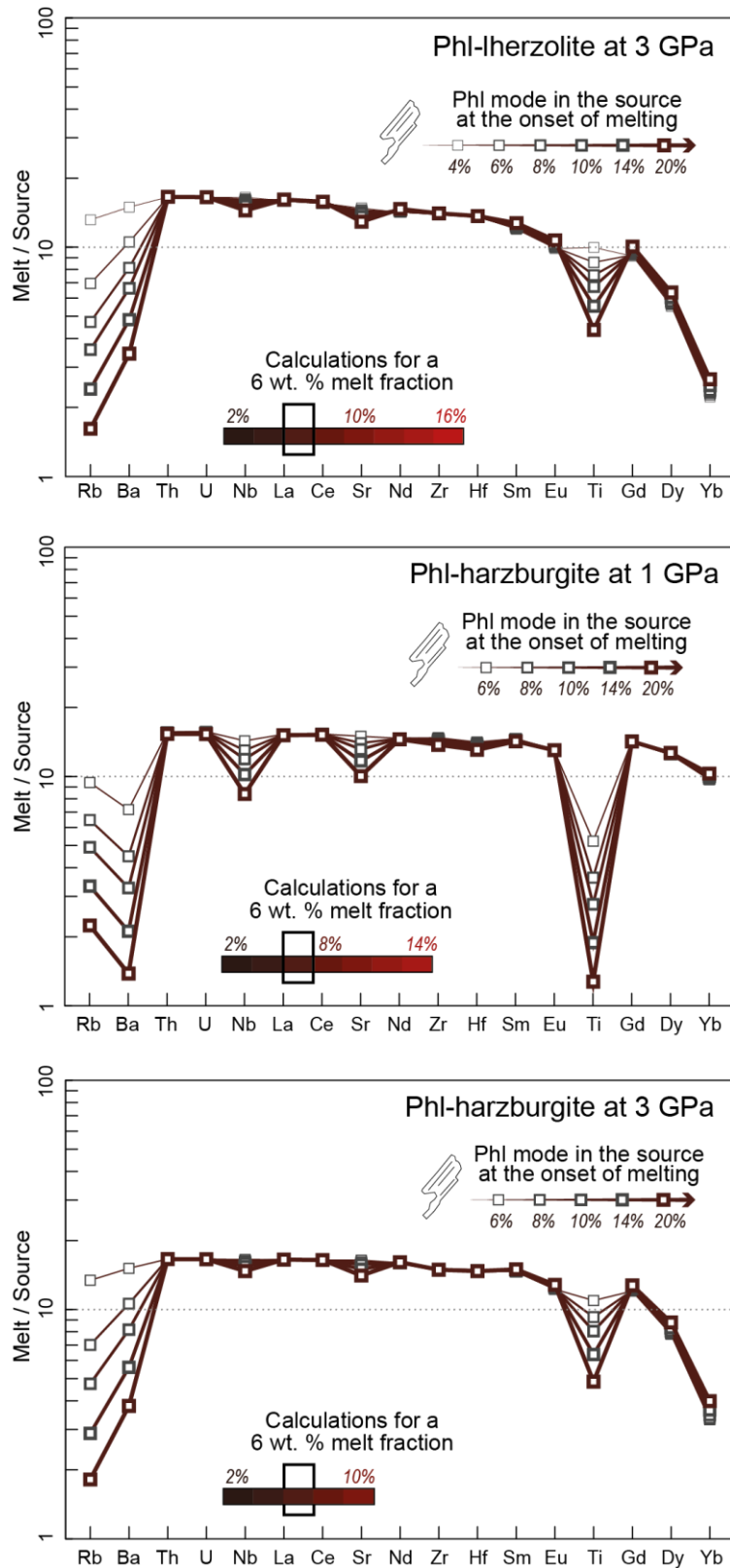
Figure S5. Multi-element diagrams showing the influence of varied proportions of phlogopite in the peridotite source at the onset of melting on the trace element concentrations of primary melts. The values were obtained running the same non-modal batch melting model displayed Figure 9 but with modified starting compositions computed as X% pure phlogopite and Y% peridotite (Phl-free, lherzolite or harzburgite) components. The mode of the lherzolite endmember was 63.9% Ol, 17.2% Opx, 9.4% Cpx, and 9.4% Grt at 3 GPa. The mode of the harzburgite endmember was 69.4% Ol, 28.9% Opx and 1.7% Spl at 1 GPa, and 67.2% Ol, 24.4% Opx, and 8.3% Grt at 3 GPa.

89 **References**

90 Adam J. and Green T. (2006) Trace element partitioning between mica- and amphibole-bearing

91   garnet lherzolite and hydrous basanitic melt: 1. Experimental results and the investigation of

92   controls on partitioning behaviour. *Contrib. Mineral. Petr.* **152**, 1–17.

93 Blundy J. and Dalton J. (2000) Experimental comparison of trace element partitioning between

94   clinopyroxene and melt in carbonate and silicate systems, and implications for mantle

95   metasomatism. *Contrib. Mineral. Petr.* **139**, 356–371.

96 Condamine P. and Médard E. (2014) Experimental melting of phlogopite-bearing mantle at 1 GPa:

97   Implications for potassic magmatism. *Earth Planet. Sc. Lett.* **397**, 80–92.

98 Green T. H., Blundy J. D., Adam J. and Yaxley G. M. (2000) SIMS determination of trace element

99   partition coefficients between garnet, clinopyroxene and hydrous basaltic liquids at 2-7.5 GPa and

100   1080-1200°C. *Lithos* **53**, 165–187.

101 Hart S. R. and Dunn T. (1993) Experimental cpx/melt partitioning of 24 trace elements. *Contrib.*

102   *Mineral. Petr.* **113**, 1–8.

103 Hofmann A. W. (1988) Chemical differentiation of the Earth: the relationship between mantle,

104   continental crust, and oceanic crust. *Earth Planet. Sc. Lett.* **90**, 297–314.

105 Kennedy A. K., Lofgren G. E. and Wasserburg G. J. (1993) An experimental study of trace element

106   partitioning between olivine, orthopyroxene and melt in chondrules: equilibrium values and

107   kinetic effects. *Earth Planet. Sc. Lett.* **115**, 177–195.

108 Klemme S., Günther D., Hametner K., Prowatke S. and Zack T. (2006) The partitioning of trace

109   elements between ilmenite, ulvospinel, armalcolite and silicate melts with implications for the

110   early differentiation of the moon. *Chem. Geol.* **234**, 251–263.

111 Shimizu H. (1980) Experimental study on rare-earth element partitioning in minerals formed at 20

112   and 30 kb for basaltic systems. *Geochem. J.* **14**, 185–202.

113 Shimizu K., Liang Y., Sun C., Jackson C. R. M. and Saal A. E. (2017) Parameterized lattice strain models

114   for REE partitioning between amphibole and silicate melt. *Am. Mineral.* **102**, 2254–2267.

115 Sun C. and Liang Y. (2014) An assessment of subsolidus re-equilibration on REE distribution among

116   mantle minerals olivine, orthopyroxene, clinopyroxene, and garnet in peridotites. *Chem. Geol.*

117   **372**, 80–91.

118 Sun C. and Liang Y. (2013) Distribution of REE and HFSE between low-Ca pyroxene and lunar picritic

119   melts around multiple saturation points. *Geochim. Cosmochim. Ac.* **119**, 340–358.

120 Sun C. and Liang Y. (2012) Distribution of REE between clinopyroxene and basaltic melt along a

121   mantle adiabat: effects of major element composition, water, and temperature. *Contrib. Mineral.*

122   *Petr.* **163**, 807–823.

123 Sweeney R. J., Green D. H. and Sie S. H. (1992) Trace and minor element partitioning between garnet

124   and amphibole and carbonatitic melt. *Earth Planet. Sc. Lett.* **113**, 1–14.

125 Tuff J. and Gibson S. A. (2007) Trace-element partitioning between garnet, clinopyroxene and Fe-rich

126   picritic melts at 3 to 7 GPa. *Contrib. Mineral. Petr.* **153**, 369–387.

127 Yao L., Sun C. and Liang Y. (2012) A parameterized model for REE distribution between low-Ca

128   pyroxene and basaltic melts with applications to REE partitioning in low-Ca pyroxene along a

129   mantle adiabat and during pyroxenite-derived melt and peridotite interaction. *Contrib. Mineral.*

130   *Petr.* **164**, 261–280.